# Preparation and Characterization of $Sb_2Se_3$ thin films

**Dissertation submitted to**
**Visvesvaraya National Institute of Technology, Nagpur**
**in partial fulfilment of the requirements for the award of the degree**

**Master of Science**

**In**

**Physics**

**by**


**AKANKSHYA PATI**

**(MS23PHY010)**


under the guidance of

**Dr. G. Hema Chandra**

**Department of Physics Visvesvaraya National Institute of Technology Nagpur (440010) India**


**May 2025**


**© Visvesvaraya National Institute of Technology (VNIT) 2009**

## Department of Physics

## Visvesvaraya National Institute of Technology, Nagpur

# Dissertation Approval Sheet

The dissertation titled "Preparation and Characterization of $Sb_2Se_3$ thin films" submitted by Ms. Akankshya Pati has been approved for the fulfilment of the degree of Masters of Science in Physics**.**

_____ _____

**(Name: Dr. G. Hema Chandra)** **(Name: )**

**Supervisor** **External Examiner**

_____

**(Name: )**

**Chairman**

Date:

Place: Nagpur

# Department of Physics

# Visvesvaraya National Institute of Technology, Nagpur

## Declaration

I, Akankshya Pati, hereby declare that this dissertation titled "Preparation and Characterization of $Sb_2Se_3$ thin films" is carried out by me in the Department of Physics of Visvesvaraya National Institute of Technology, Nagpur. The work is original and has not been submitted earlier whole or in part for the award of any degree/diploma at this or any other Institution / University.

Akankshya Pati
Date:

## Certificate

This to certify that the dissertation titled "Preparation and Characterization of $Sb_2Se_3$ thin films" is submitted by Akankshya Pati in partial fulfilment of the requirements for the award of the degree of Master of Science in Physics, VNIT Nagpur. The work is comprehensive, complete and fit for final evaluation**.**

**Dr. G. Hema Chandra**
Professor
Department of Physics
VNIT, Nagpur

Head, Department of Physics
VNIT, Nagpur
Date:

# Department of Physics

# Visvesvaraya National Institute of Technology, Nagpur

## Non-Plagiarism Certificate

Certified that M.Sc. dissertation titled "Preparation and Characterization of $Sb_2Se_3$ thin films" submitted by Akankshya Pati, Enrollment no. MS23PHY010 And ID No. 30145 has been checked for plagiarism using TURNITIN and overlap is found within prescribed limits. A summary of report given below:

| ORIGINALITY REPORT | | | |
|---|---|---|---|
| 8% | 5% | 6% | % |
| SIMILARITY INDEX | INTERNET SOURCES | PUBLICATIONS | STUDENT PAPERS |
| PRIMARY SOURCES | | | |


**Akankshya Pati**
(MS23PHY010)
ID No. 30145

**Dr. G. Hema Chandra**
Professor,
Department of Physics

# Acknowledgements

I would like to express my sincere gratitude to **Dr. G. Hema Chandra**, Professor, Department of Physics, Visvesvaraya National Institute of Technology, Nagpur, for providing me the opportunity and for his guidance to carry out the M.Sc. project under him. It was a great experience for learning and gained invaluable insight into the semiconductor devices and their fundamentals.

I would like to thank **Dr. B.R. Sankapal**, Head of Department of Physics, VNIT and **Dr. Prem Lal Patel**, Director, VNIT, for providing me necessary facilities for the completion of my project work in a good way.

I am extremely grateful to **Ms. Shreosi Mukherjee** and **Mr. Yashpal Pawar**, Research scholars, Department of Physics, VNIT, for his relentless support and valuable advice throughout the duration of my project.

I would like to thank my classmate **Aman Kumar Gill** for his support and help.

I am extremely grateful to my parents and family members, without their support and nurturing, the completion of my project would not have been possible.

**AKANKSHYA PATI**

# ABSTRACT

Antimony selenide ($Sb_2Se_3$) thin films were synthesized via stacked elemental deposition of Cu/(Sb/Se) x3 /Cu through electron beam evaporation on glass substrates, followed by thermal annealing in an argon atmosphere inside a tubular furnace, varying temperatures and selenium content. Annealing the precursors at temperatures greater than 225 °C led to instability in the resulting films, indicating that such conditions were not optimal. Compositional analysis carried out through Energy dispersive X-ray spectroscopy showed the $Sb_2Se_3$ sample selenized at 225 ºC with selenium content of 30 mg for 15 minutes at 600 mbar pressure to possess Se/Sb ratio of 1.49, which is near to desired stoichiometry. Structural analysis through X-ray diffraction and Raman confirmed the presence of orthorhombic phase of $Sb_2Se_3$ in all samples. Single phase $Sb_2Se_3$ was grown irrespective of changing temperature and varying selenium content. Surface morphology was analysed of the films selenized at 225 °C through Field emission Scanning electron microscope, which showed uniform and densely packed grains with an average size of 554 nm. Optical analysis, carried out through UV-Vis NIR spectrophotometer, revealed a direct band gap of 1.07 eV for sample selenized at 225 °C. The film thickness was about 480 nm. Hall-effect measurements confirmed *p*-type conductivity with a hole concentration of $3.8 \times 10^{17}$ $cm^{-3}$, mobility of $1.2 \times 10^{3}$ $cm^2/Vs$ and resistivity of $1.3 \times 10^{-2}$ $\Omega$ cm.

# CONTENTS

Abstract

Contents

List of Figures

List of Tables

List of Abbreviations

List of Symbols

**CHAPTER 1: INTRODUCTION**

**1.1. Energy consumption**

**1.2. Energy sources**

**1.2.1. Renewable energy sources**

**1.3. Solar cell**

**1.3.1. Photovoltaic effect**

**1.3.2. Energy band diagram**

**1.3.3. IV Characteristics**

**1.3.4. Generations of solar cell**

**1.3.4.1. First Generation solar cell**

**1.3.4.2. Second Generation solar cell**

**1.3.4.2.1. Thin film solar cell**

**1.3.4.2.2. Homojunction solar cell**

**1.3.4.2.3. Heterojunction solar cell**

**1.4. Optical Absorption**

**1.5. Absorber layer of solar cell**

**1.6. $Sb_2Se_3$ compound as an absorber layer of solar cell**

**CHAPTER 2: LITERATURE REVIEW**

**2.1. Experimental research**

**2.1. Computational research**

**CHAPTER 3: EXPERIMENTAL WORK**

**3.1. Thin film deposition by Electron beam evaporation method**

**3.1.1. Vacuum Coating Unit**

**3.1.1.1. Rotary pump and diffusion pump**

**3.1.1.2. Pirani Gauge and Penning Gauge**

**3.1.2. Quartz Thickness Monitor (QTM)**

**3.1.3. Other elements of electron beam system**

**3.2. Fabrication of $Sb_2Se_3$ thin films**

**3.2.1. Substrate Preparation**

**3.2.2. Vacuum generation and deposition**

**3.2.3. Stack Variation and film composition**

**3.3. Annealing of precursor films**

**3.4. Characterization Methods**

**3.4.1. X-ray Diffraction method**

**3.4.1.1. Bragg's Law**

**3.4.1.2. Debye Scherrer formula**

**3.4.1.3. X-ray Diffractometer**

**3.4.2. Raman Spectroscopy**

**3.4.3. UV-Visible-NIR Spectroscopy**

**3.4.4. Scanning Electron Microscopy and EDX**

**3.4.5. Optical Profilometer**

**3.4.6. Hall effect measurement system**

**CHAPTER 4: RESULTS AND DISSCUSION**

**4.1. Compositional analysis**

**4.2. Structural analysis**

**4.2.1. XRD analysis**

**4.2.2. Raman analysis**

**4.3. Morphological analysis**

**4.4. Thickness measurement**

**4.5. Optical analysis**

**4.6. Electrical properties**

**CHAPTER 5: CONCLUSION**

**5.1. Summary and conclusion**

**5.2. Future Scope**

## LIST OF FIGURES


| Figure no. | Title of Figure | Page no. |
|---|---|---|
| 1 | Primary Energy Consumption. Reference year 1984.Source: International Energy Agency (IEA) | 1 |
| 2 | Energy consumption of servers and data centers in Germany over years 2010-2017(Source- Borderstep) | 2 |
| 3 | U.S. Primary energy consumption by energy sources 2012(Source: Energy Information Adminstration) | 2 |
| 4 | India Renewable energy sources list 2018 (Source: Britannica) | 4 |
| 5 | Solar cell structure | 5 |
| 6 | Band gap of a semiconductor | 6 |
| 7 | Energy band diagram of solar cell | 6 |
| 8 | IV characteristics of Solar cell | 7 |
| 9(a) | Heterojunction solar cell Before reaching equilibrium | 10 |
| 9(b) | Heterojunction solar cell after reaching equilibrium | 10 |
| 10 | Optical absorption for (i) $h\nu > E_g$ (ii) $h\nu = E_g$ (iii) $h\nu < E_g$ | 12 |
| 11 | Various parameters of solar cell | 13 |
| 12 | Crystal structure of $Sb_2Se_3$ | 14 |
| 13(a) | Schematic diagram of Rotary pump | 19 |
| 13(b) | Mechanism of Rotary pump | 19 |
| 14 | Mechanism of diffusion pump | 20 |
| 15 | Working mechanism of Pirani gauge | 21 |
| 16 | Penning gauge working principle | 22 |

| | | |
|---|---|---|
| 17(a) | Quartz crystal monitor outside | 23 |
| 17(b) | view Quartz crystal monitor inside view | 23 |
| 18 | Crucible, Electron gun and magnets inside the chamber | 25 |
| 19 | Ultra sonication of glass substrate | 26 |
| 20 | Substrate holder | 26 |
| 21 | Electron beam evaporation method set up | 27 |
| 22 | Stacking order of precursor film | 27 |
| 23 | Cu/$Sb_2Se_5$/Cu thin film precursors deposited by e- beam | 28 |
| 24 | Horizontal Tubular Furnace | 29 |
| 25 | Graphite box with Graphite plate | 29 |
| 26 | X-ray diffraction by lattice surface | 30 |
| 27 | X-ray diffractometer | 32 |
| 28 | Various vibrational states | 33 |
| 29 | Raman Spectroscopy | 33 |
| 30 | Schematic of Raman Spectroscopy | 33 |
| 31 | Schematic diagram of double beam spectrophotometer | 34 |
| 32 | UV-Visible-NIR Spectroscopy apparatus | 35 |
| 33 | Representation of hall effect in a p-type semiconductor | 35 |
| 34 | Current and voltage presentation in Hall effect | 37 |
| 35 | Schematic diagram of Scanning electron microscope | 38 |
| 36 | Procedure of Scanning electron microscope | 39 |
| 37 | Various signals generated from the specimen | 40 |
| 38 | SEM equipped with EDS | 40 |
| 39 | Working of optical Profilometer | 41 |

| | | |
|---|---|---|
| 40 | Non-contact optical Profilometer | 42 |
| 41 | EDS spectrum of Cu/$Sb_2Se_5$/Cu thin film annealed with 30 mg selenium powder at 225 ºC for 15 minutes at 600 mbar | 44 |
| 42 | XRD pattern of $Sb_2Se_3$ thin film annealed at various temperatures and with different selenium content.4 | 45 |
| 43 | Raman spectra of $Sb_2Se_3$ thin films annealed at various temperatures and with different selenium content | 46 |
| 44 | SEM image of $Sb_2Se_3$ annealed at 200 ºC with 30 mg selenium for 15 minutes at 600 mbar pressure | 47 |
| 45 | SEM image of $Sb_2Se_3$ annealed at 225 ºC with 30 mg selenium for 15 minutes at 600 mbar pressure | 48 |
| 46 | SEM images of $Sb_2Se_3$ soft annealed at 225 ºC for 15 minutes at 600 mbar pressure | 48 |
| 47 | Surface profile and thickness of $Sb_2Se_3$ thin film selenized with 30 mg of Se at 225 ºC for 15 minutes a d 600 mbar pressure by optical profilometer | 50 |
| 48 | Reflectance spectra of $Sb_2Se_3$ thin films annealed at different parameters | 51 |
| 49 | Tauc plot of $Sb_2Se_3$ thin films annealed in presence of 30 mg selenium 200 ºC for 15 min at 600 mbar using Kubelka-Munk function | 52 |
| 50 | Tauc plot of $Sb_2Se_3$ thin films annealed in presence of 30 mg selenium 225 ºC for 15 min at 600 mbar using Kubelka-Munk function | 52 |
| 51 | Tauc plot of $Sb_2Se_3$ thin films soft annealed at 225 ºC for 15 min at 600 mbar using Kubelka-Munk function | 53 |

## LIST OF TABLES


| Table no. | Title of Table | Page no. |
|---|---|---|
| 1 | Various parameters of solar cell | 8 |
| 2 | Structure and property of $Sb_2Se_3$ compound | 14 |
| 3 | Classification of Vacuum | 18 |
| 4 | Thickness and rate of deposition of Cu/$Sb_2Se_5$/Cu precursor thin film | 28 |
| 5 | Cu/$Sb_2Se_5$/Cu thin films annealed at different parameters | 30 |
| 6 | Chemical composition of $Sb_2Se_3$ thin films annealed at different parameters | 43 |
| 7 | Crystallite size of $Sb_2Se_3$ thin film annealed at various temperatures and with different selenium content | 45 |
| 8 | Thickness measurements of $Sb_2Se_3$ thin films annealed at different parameters | 49 |
| 9 | Energy band gap of $Sb_2Se_3$ thin films annealed at different parameters | 51 |
| 10 | Electrical properties of $Sb_2Se_3$ thin films annealed at different parameters | 53 |

## LIST OF ABBREVIATIONS

| Abbreviation | Full form |
|---|---|
| $Sb_2Se_3$ | Antimony Selenide |
| Cu | Copper |
| Sb | Antimony |
| Se | Selenide |
| eV | electron-Volt |
| PVD | Physical vapour deposition |
| QTM | Quartz thickness monitor |
| XRD | X-ray Diffraction |
| EDS | Energy Dispersive Spectroscopy |
| UV-Vis-NIR | Ultra Violet-Visible-Near Infrared Radiation |
| SEM | Scanning Electron Microscope |
| $CO_2$ | Carbon dioxide |
| CdS | Cadmium sulfide |
| ZnS | Zinc sulfide |
| ZnO | Zinc oxide |

## LIST OF SYMBOLS

| Symbol | Meaning |
|---|---|
| $E_c$ | Conduction band energy |
| $E_v$ | Valence band energy |
| $E_g$ | Energy band gap |
| Å | Angstrom ($10^{-10}$) |
| θ | Bragg's angle |
| K | Kelvin |
| λ | Wavelength |
| Δf | Change in frequency |
| Δm | Change in thickness |
| q | charge |
| t | Thickness of the sample |
| V | Voltage |

# CHAPTER 1: INTRODUCTION

## 1.1. Energy Consumption

In the twenty-first century, enhancing energy efficiency is a major global requirement, influencing industries and communities worldwide. During 1984-2004 energy consumption is increased by 49% with 43% carbon dioxide emission [1]. In 2004, the net power consumption embodied in household, government, and investment are 7749, 874, and 2009 Mtoe (million tons of oil equivalent), respectively. In fact, worldwide energy use is projected to increase by nearly 50% by 2050, according to energy experts. According to the U.S. Energy Information Administration, fossil fuels still account for over 80% of global energy use i.e. most of the modern civilization have become dependent on fossil fuels for decades [1]. These energy consumption data indicate a rising trend in the use of energy resources.

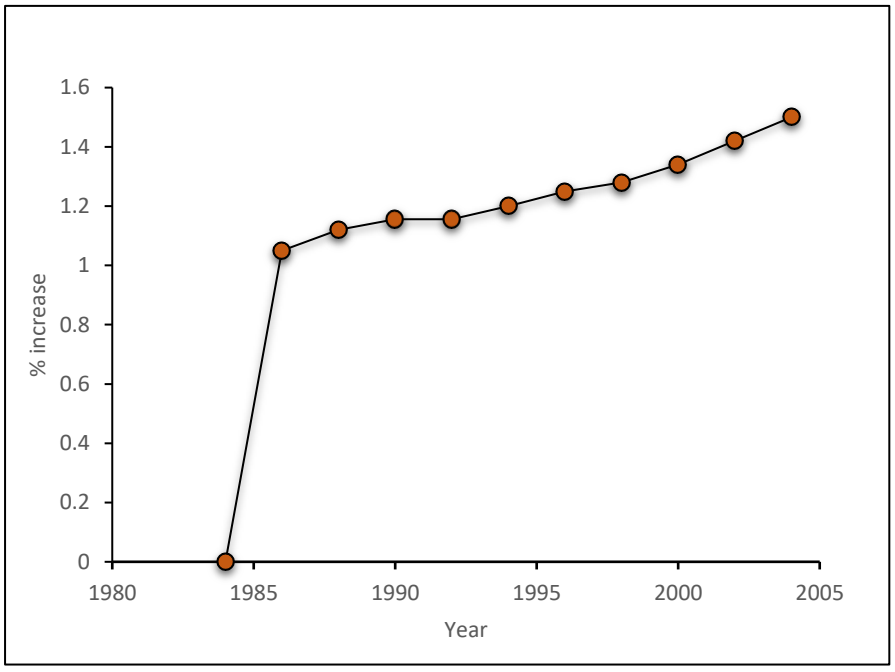


**Figure 1: Primary Energy Consumption. Reference year 1984.Source: International Energy Agency (IEA)**

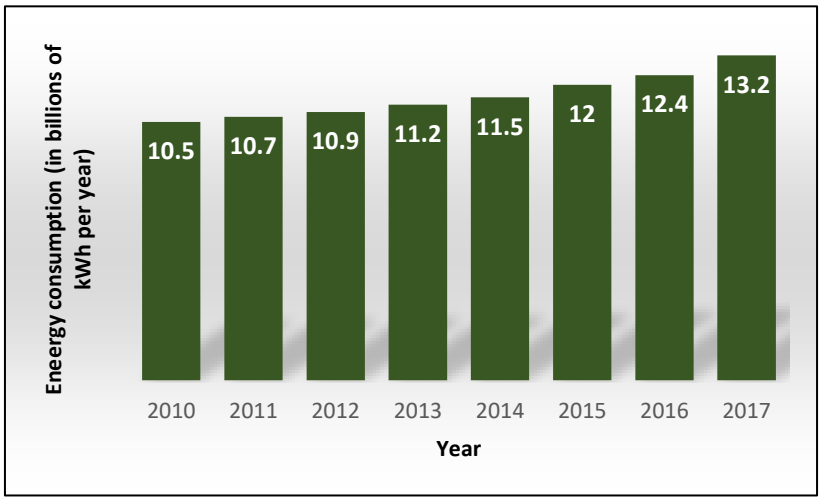


**Figure 2: Energy consumption of servers and data centers in Germany over years 2010-2017(Source- Borderstep)**

## 1.2 Energy Sources

Energy source powers the economical growth along with industrial development by attaining the basic needs of mankind. The Sun is considered as the primary source of energy. The energy which get stored in materials known as fuel.The energy can be classified based upon its replenishment as renewable(non-conventional) energy resources and non-renewable(conventional) energy resources.

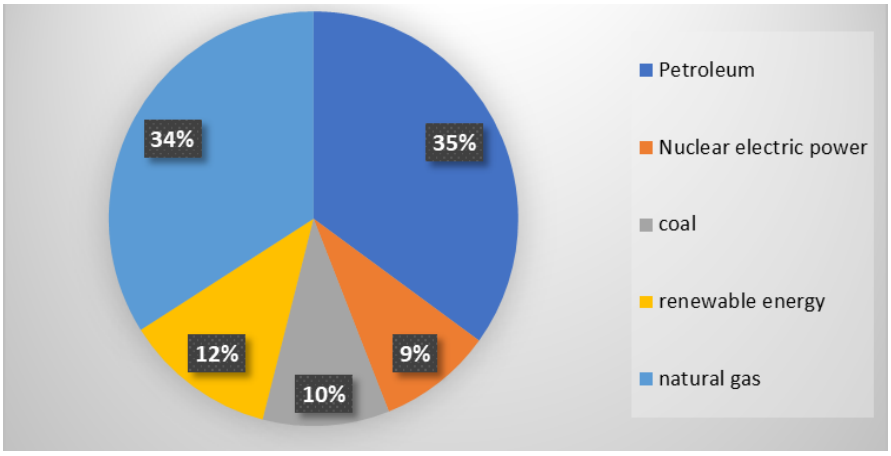


**Figure 3: U.S. Primary energy consumption by energy sources 2012(Source: Energy Information Adminstration)**

Energy sources have a great impact on the environment. The estimation of IEA says that the consumption of fossil fuels leaded to 33.1% $CO_2$ emission worldwide which

could be the reason of increase in greenhouse gas, air pollution and the climate change [1].Increase in population will demand more consumption of energy.To fulfill the energy demand, instead of conventional sources, non-conventional energy sources have to be used. Shifting to renewable energy sources (non-conventional energy sources) reduces the side effects and lead to better consequences. Furthermore,renewable energy sources are cost effective, environment friendly and designed with great technologies which takes it one step ahead. Efficient energy sources, secured energy souces and transition to renewable energy sources, are the challenges and opportunities that need to be taken care of [2].

### 1.2.1 Renewable Energy Sources

Renewable energy is a reliable and sustainable form of power that originates from natural sources and is continuously regenerated, also labeled as clean or green energy. These energy sources are directly or indirectly dependent upon sun. These are classified as Solar energy (solar radiation from sun), Geothermal energy (hot springs), Biomass energy (bio fuels), Wind energy (wind power), Hydroelectric energy (rivers), Tidal energy (tides of ocean) etc.

**Solar Energy:**The solar energy received from sun to Earth surface is more than the expected requirement of the mankind. It is a sustainable source and leads to no $CO_2$ emission. Photovolatic cells and solar thermal systems converts the solar energy to electrical energy. This is a currently expanding renewable energy source among all. This is also a very common available energy source. The consistent decrease in its price is making it more affordable. In past two decades the annual growth rate of solar cell is nearly 30 %. This implies an exponenetial growth worldwide.[2].

**Geothermal Energy:**It is the energy that is formed and stored inside the Earth's crust in the form of heat energy.Though the availability is more than the requirement but the extraction of it is difficult than any other sources.Although the difficulties remain it has been proved as a viable alternative and also reduces environmental pollutions. Its implementation has been increased in past three decades implying its sustainability [3].

**Biomass Energy:**Biomass energy conversion process involves the synthesis of organic molecules which break down from its complex structure.The material may be organic matter, algae, wastes, living organisim wastes, agricultural residues etc.[4]. However, there

are still concerns regarding the reduction of biodiversity and the emission of greenhouse gases.

**Wind Energy:**The wind is formed by differennce in temperatures between two regions. It is estimated that nearly 10 milion MW of energy is availble in earth at any instataneous time[5].Wind turbine technology is used to convert this into energy. This is classified into *Onshore wind energy*( Operated on land) and *Offshore wind energy*(Operated inside waterbodies). It can be more efficient by increasing height, incresing power factor and choosing efficient sites for it. Fluctuation in the wind, cost effectiveness are the chalenging factor in implemanting this [5].

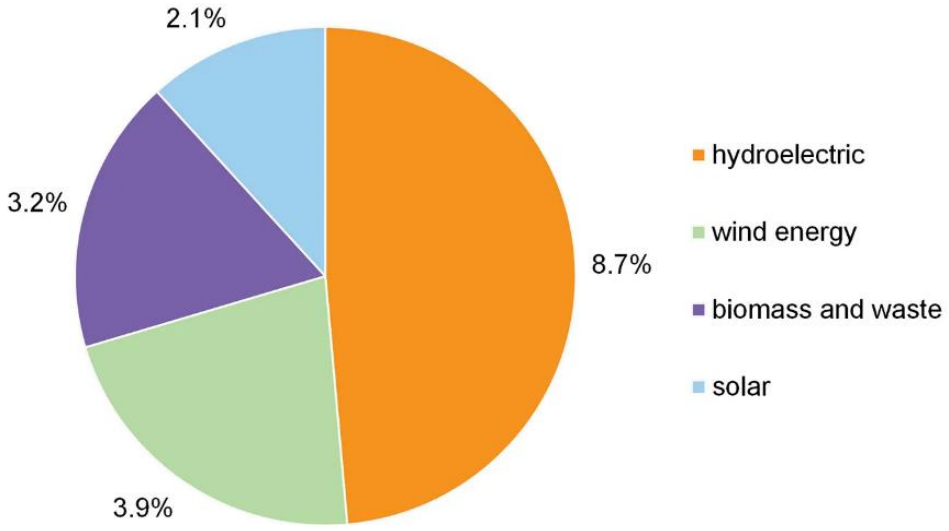


**Figure 4: India Renewable energy sources list 2018 (Source: Britannica)**

## 1.3 Solar Cells

Solar cell, also known as photovoltaic cell is the unit of solar energy. It converts solar energy to electrical energy. This acts upon the principle of Photovoltaic effect.

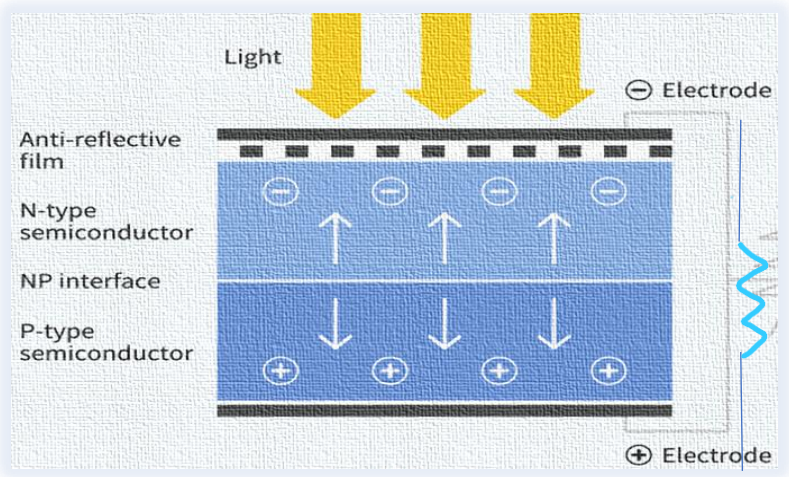


**Figure 5: Solar cell structure**

It is basically a p-n junction followed by ohmic contacts on both sides and anti-reflection coating on the exposure side. It is a sustainable unit of solar energy which can be available in different states (solid, liquid and gaseous), though maximum efficiency is obtained by solid medium. It has taken on a significant role in the global clean energy [6].

### 1.3.1 Photovoltaic Effect

In a *p-n* junction *p*-side is rich in positive charge carriers and *n*-side is rich in negative charge carriers. The electrons from *n*-side and hole from p-side prefer to move towards respective opposite sides due to concentration gradient across the junction. This leads to donor and acceptor immobile ions which generates an electric field near the junction. More and more electron travel to *p*-side and holes move to *n*-side of the junction. That gives rise to a potential barrier across the junction [6].

The photovoltaic effect can be explained by following steps.

**1.Generation of charge carriers in response to photons**

The photon gets absorbed and electron jumps from lower excited state $E_i$ to higher excited state $E_f$. The condition for the absorption is that the photon's energy must satisfy $h\nu \geq E_f - E_i$. The valence band contains electrons bound to atoms, while the conduction band consists of energy levels where electrons can move freely and conduct electric current. The photon energy should be greater than $E_g$ for absorption. The electron leaves a void behind which acts as a hole. The absorption of photon leads to create an electron-hole pair [6].

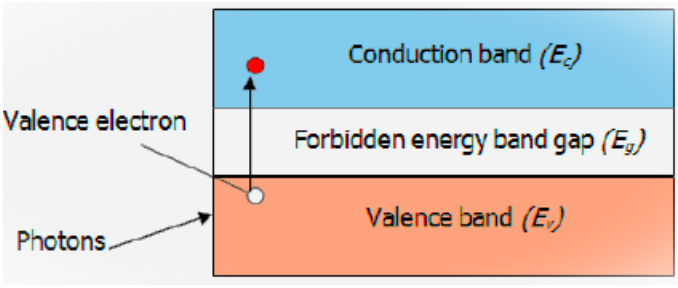


**Figure 6**: **Band gap of a semiconductor**

**2.Separation of photo-generated charge carriers in the junction**

A solar cell is designed in a way so that the electron and hole can reach their respective membrane before they recombine and it must be shorter than their life time**.** As the life time of charge carriers are very small, they should reach at membrane before they recombine otherwise it will not be able to provide current.

**3.Collection of charge carriers at the junction terminal**

The electron and hole may recombine after crossing the circuit. These extracted carriers have electrical contacts by their side which converts solar energy to electrical energy [6].

**1.3.2 Energy band diagram**

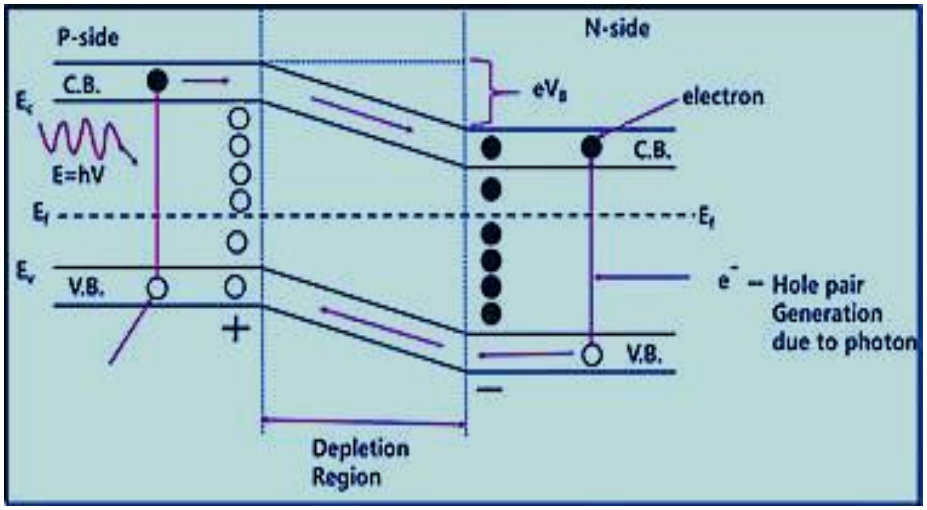


**Figure 7: Energy band diagram of solar cell**

A bandgap is the energy gap between the valence band and the conduction band of a material. When *p*-type and *n*-type semiconductors come in contact their fermi level shifts

and tends to attain a common energy level, known as equilibrium. To arrange in equilibrium the bands bend in respective directions. When a photon with enough energy gets absorbed, it excites the electron to jump from valence band to conduction band forming an electron-hole pair. The electron moves from *p*-side to *n*-side and the hole from *n*-side to *p*-side and it gives the current in output. As the current is due to minority charge carriers it is also known as minority charge carrier device. In case of no biasing the built-in potential($eV_0$) is the potential difference between the conduction bands of *n*-type and *p*-type. In forward bias it is decreased and in reversed bias it gets increased by a factor which depends upon the applied voltage [7].

### 1.3.3. IV Characteristics

In application of light there are electron-hole pair generation which gets accumulated at respective sides. When both sides are not connected, there is infinite resistance which obtains the maximum voltage i.e. open circuit voltage ($V_{oc}$). When we connect both the sides zero resistance is there, so the maximum current is gained known as short circuit current ($I_{sc}$). The zero resistance is an ideal concept so there must be some resistance in between which leads to a curve lies between $V_{oc}$ and $I_{sc}$. The maximum power gained by a solar cell is the maximum area under the curve [7].

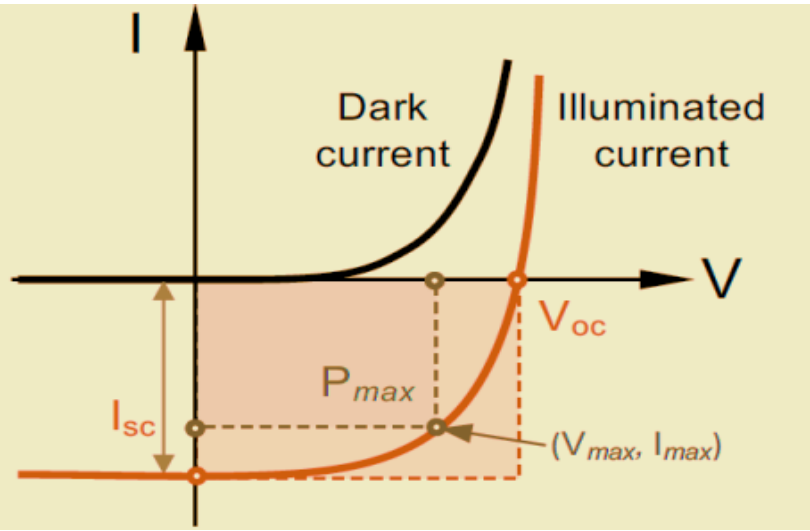


**Figure 8: IV characteristics of Solar cell**

As per the figure, here are some parameters of solar cell-

**Table 1: Various parameters of solar cell**

| | |
|---|---|
| **Maximum power ($P_{max}$)** | $V_{max} \times I_{max}$ |
| **Fill factor** | $(V_{max} \times I_{max}) / (V_{oc} \times I_{sc})$ |
| **Efficiency** | $P_{max} / P_{incident}$ |

### 1.3.4. Generations of Solar cell

#### 1.3.4.1 First-Generation Solar cell

The most commonly used solar cells are of first generation due to their high promising conversion efficiencies. They are generally wafer based and classified into: (i) **Single crystal solar cell** (17-18 % efficiency) **and** (ii) **polycrystalline solar cell** (12-13% efficiency). The polycrystalline solar cells are more economical but less efficient yet believed to occupy 48% of solar cell production in 2008 [8].

#### 1.3.4.2. Second-Generation of Solar cell

These solar cells are more advanced with technologies and aim to improve upon first-generation solar cells. Thin film solar cells along with amorphous silicon solar cell are introduced in this generation. Thin film solar cell stands out due to its thin absorbing layer in comparison to absorbing layer of first-generation solar cell (Si wafer solar cells have ~350 μm thick absorbing layer) [8]. These are more economical and enriched in technology. Some of the second-generation solar cells are a-Si, CdTe, CIGS. They are cost effective and yet efficient. The efficiency lies between 15-23 %. This generation also has dye sensitized and multijunctional solar cells, demonstrating flexibility [9].

##### 1.3.4.2.1. Thin film Solar cell

Thin film solar cell contains thin photovoltaic material deposited on a substrate. To increase the photovoltaic phenomena and to reduce the diffusion length the absorption layer has to be minimized. Though it was challenging but in thin film solar cell with less

thickness of absorption layer and yet remarkable efficiency was obtained. Today thin film solar cells share 55% of market reservation [10].

It consists of 4 layers-

(i) **Front Ohmic Contact:** All the solar cells have metal-semiconductor junction at the front side to connect with external circuit and to let current flow. To make it function properly low resistance contact is used, known as ohmic contact. The area of contacts is minimized by making finger like patterns which enhances the exposure for photovoltaic effect and also collect charges significantly. The contact resistances of these junction are negligible in comparison to bulk resistances of semiconductor [6].

(ii) **Window layer:** This layer is supposed to have higher band gap, small thickness and lower series resistance for high optical throughput. The high band gap allows the light to pass through it and do not get absorbed. It assists formation of more exciton [11].

(iii) **Absorber layer:** This is the core of solar cell where the light gets absorbed and form exciton pair to generate photocurrent. This layer is selected among the semiconducting materials which have bandgap accorded with photon rich spectrum of solar cell [12].

(iv) **Back Ohmic contact:** This layer is on bottom of the solar cell made of up fine metal grid to collect photo carriers and to maintain the circuit. This covers entire back of absorber solar cell and completes the circuit.

Thin film solar cells can be classified into

(i) **Homojunction solar cell**

(ii) **Heterojunction solar cell.**

#### 1.3.4.2.2. Homojunction Solar cells

Homojunction solar cells are formed when both window layer and absorber layer are of same semiconducting material doped differently to form *p*-type and *n*-type. Lattice mismatching is not present in homojunctions solar cell. Firstly, homojunction solar cell was configurated as *p*-*i*-*n* structure. The efficiency was first measured to be 6% and then gets boosted by using different materials and doping levels. The intrinsic material is used to reduces lattice strains and defect densities and exciton recombination [7].

### 1.3.4.2.3. Heterojunction Solar cells

The metallurgical interface of *p*-type and *n*-type of two different semiconductor forms heterojunction. Among these two layers *p*-type acts as absorber layer and *n*-type acts as window layer. The layers exhibit different parameters like band gap, work function, electron affinities, lattice parameters, thermal expansion coefficient etc. [13]. There are some criterions for developing a better heterojunction are

i. Electron affinity of two semiconductors should be compatible (to avoid energy discontinuities).
ii. Lattice constants of two materials should be nearly equal (to avoid interfacial states).
iii. Thermal coefficient of materials should be close to each other (to avoid interfacial states) [13].

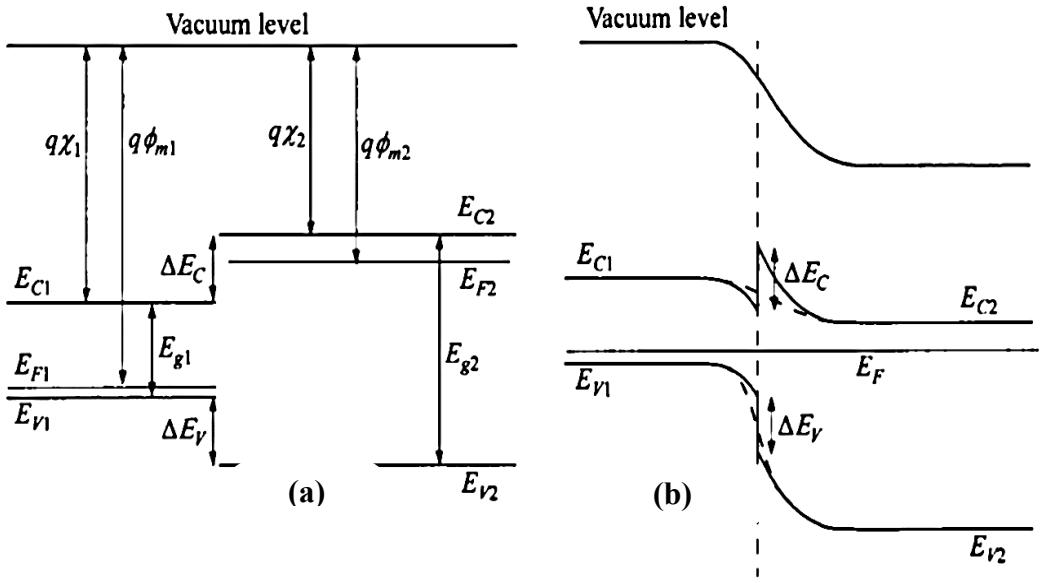


**Figure - 9(a) Before reaching equilibrium; (b) After reaching equilibrium**

Some parameters used in the figure-

i. **Vacuum leve**l-It is considered as the reference level. It represents an electron outside the material. It helps in understanding how the energy bands align at their interface. The difference in vacuum levels of the materials plays a key role in how the device works [13].

ii. **Fermi level ($E_f$)**-It indicates the highest energy of electron in a material at that given temperature.

iii. **Electron affinity ($q\chi$)**-It is the difference between the lowest energy in the conduction band and the vacuum level. When a neutral atom gains an extra electron by forming into a negative ion the energy change is the electron affinity.

iv. **Work function ($q\phi$)**- It is the energy difference between the vacuum level and the fermi level of a material. The minimum energy required to release an electron from the surface to vacuum level is stated as work function.

From the figure, the energy band difference ($\Delta E_g$) is given by,

$$\mathbf{\Delta E_g = E_{g1} - E_{g2}} \quad \text{…. (1)}$$

$$\mathbf{\Delta E_c = q\,(\chi_1 - \chi_2)} \quad \text{…. (2)}$$

$$\mathbf{\Delta E_v = E_{g1} + q\,\chi_1 - (Eg_2 + q\,\chi_2) = \Delta E_g - \Delta E_c} \quad \text{…. (3)}$$

Where $\Delta E_c$ and $\Delta E_v$ are the energy difference between conduction band and valence band respectively [13].

If $V_{b1}$ and $V_{b2}$ are the potential at equilibrium in *p*-type and *n*-type with doping concentration $N_1$ and $N_2$,

Total build-in potential is given by,

$$\mathbf{V_{bi} = V_{b1} + V_{b2}} \quad \text{…. (4)}$$

$$\mathbf{V_{b1} = \frac{\varepsilon_1 N_1 (V_{bi} - V)}{\varepsilon_1 N_1 + \varepsilon_2 N_2}} \quad \text{…. (5)}$$

and

$$\mathbf{V_{b2} = \frac{\varepsilon_2 N_2 (V_{bi} - V)}{\varepsilon_1 N_1 + \varepsilon_2 N_2}} \quad \text{…. (6)}$$

## 1.4. Optical Absorption

When a photon with enough energy gets absorbed, the covalent bond is broken and electron-hole pair is formed which converts optical energy to electrical energy.

i. When $h\nu > E_g$: The incident light gets absorbed. An exciton is generated of energy $E_g$ and rest energy is released as heat energy.

ii. When $h\nu = E_g$: An exciton is created of energy $E_g$.

iii. When $h\nu < E_g$: There will be no absorption of incident photon. The energy may get trapped by some impurities or defects present in forbidden energy band gap [7].

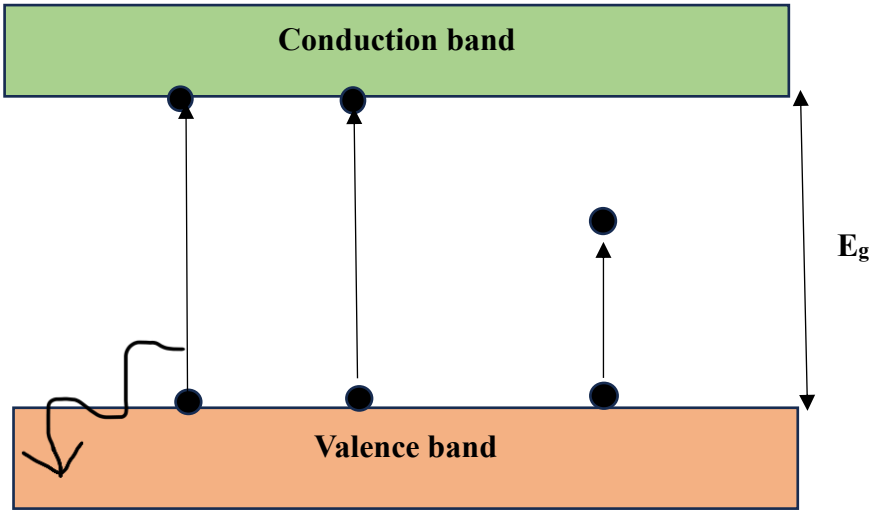


**Figure 10: Optical absorption for (i) $h\nu > E_g$ (ii) $h\nu = E_g$ (iii) $h\nu < E_g$**

In case of (i) and (ii) both transitions come under intrinsic transitions (band to band transitions). When the energy is less it gets absorbed by energy states in forbidden energy gap caused by impurities or defects, known as extrinsic transitions.

## 1.5 Absorber layer of solar cell

It is known as the heart of the solar cell. It is responsible for capturing light and in response let electrons to conduction band and create current. Absorber layer is made up of semiconducting materials possessing low band-gap energies i.e. the band-gap energies coincide with photon-rich region of solar-spectrum. Absorber layer thickness is a major parameter which affects the efficiency of solar cell. An optimized thickness of absorber layer is suitable for use. If the thickness of absorber layer is increased the charge carrier takes more time to reach the ohmic contacts and there are chances of recombination. According to research, the performance of solar cells. The open circuit voltage, the short circuit current, the fill factor, get affected by the absorber layer thickness. It is necessary to reduce the thickness of absorber layer by maintaining the conventional performance, so an optimization is needed [14]. The absorber layer can also be doped to achieve the desired efficiency and to explore more characteristic parameters. Moreover, it should be cost

effective, non-toxic, thermally and chemical stable and abundant. Some popular absorber layers of solar cells are –

(i) CIGS (Copper Indium Gallium Di selenide) absorber layer has band-gap of 1.01 to 1.68 eV. Research says that the maximum efficiency obtained till now with CIGS absorber layer (2 μm) is 20.3 % by considering the band gap 1.48 eV [15].

(ii) CdTe (Cadmium telluride) absorber layer has band gap of value near 1.45 eV at room temperature. *p*-type doping and non-*p*-type doping can effectively increase the performance of this material. Through fabrication the maximum efficiency is obtained till today to be nearly 22% [16].

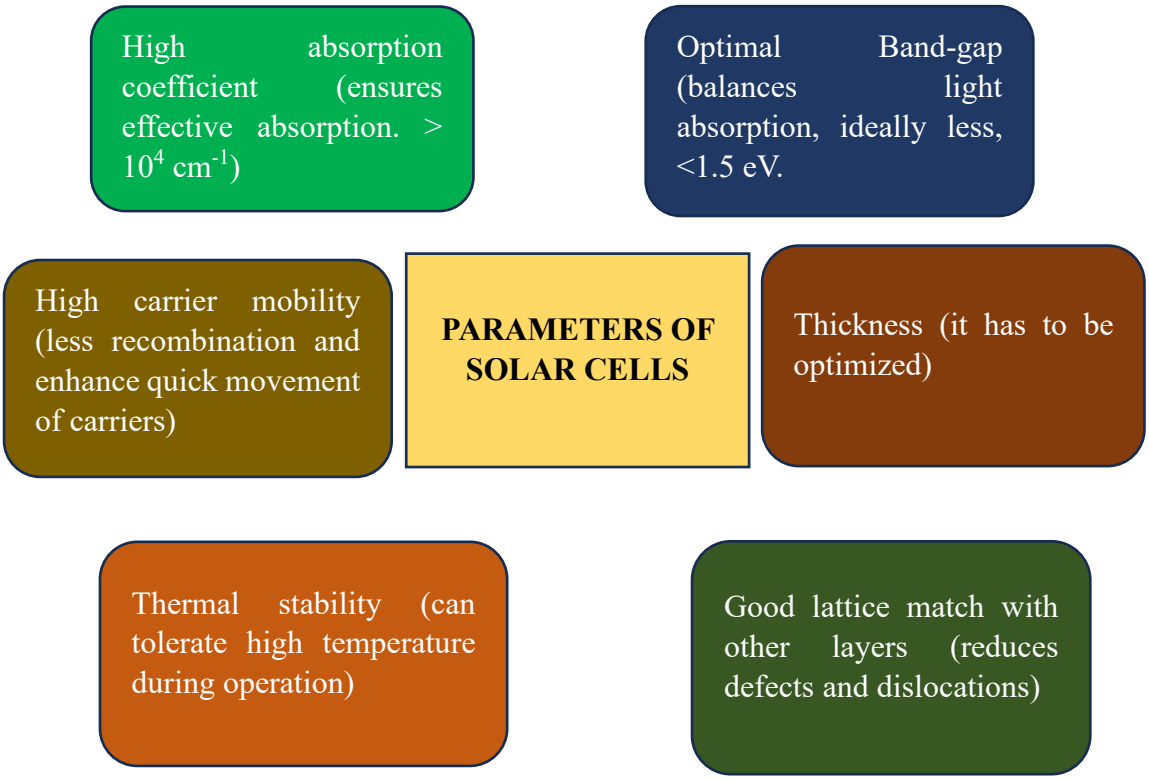
High absorption coefficient (ensures effective absorption. > $10^4$ $cm^{-1}$)
Optimal Band-gap (balances light absorption, ideally less, <1.5 eV.
High carrier mobility (less recombination and enhance quick movement of carriers)
PARAMETERS OF SOLAR CELLS
Thickness (it has to be optimized)
Thermal stability (can tolerate high temperature during operation)
Good lattice match with other layers (reduces defects and dislocations)

**Figure 11: Parameters of solar cell**

## 1.6. $Sb_2Se_3$ as an absorber layer of solar cell

$Sb_2Se_3$ is a semiconductor binary compound in the V-VI family. The compounds formed by elements of the group V(pnictogens) and the elements from the group VI (chalcogens) are known for their diversity and impressive properties. The main obstacle arises in the production of solar cell is to deal with the toxicity and cost of the material.

So, in last few decades researcher exert themselves on binary compounds and focused on high conversion efficiency. $Sb_2Se_3$ has got a great attention in the photovoltaic absorber due to its high conversion efficiency and suitable band gap. Recent research shows that high quality ZnO:Al/ZnO/CdS/TiO2/Sb2Se3/MoSe2/Mo shows 9.2% power conversion efficiency. According to Shockley-Queisser model this material efficiency can go up to 33.3% [17]. Due to low cost, estimated high conversion efficiency, high absorption coefficient and satisfactory bandgap it has been proved itself an appropriate absorber layer in the field of photovoltaic application.

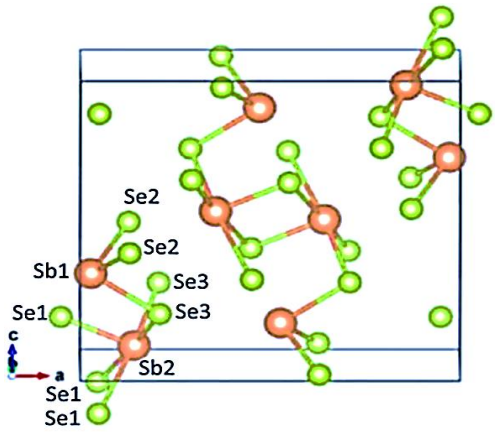


**Figure 12: Crystal structure of $Sb_2Se_3$**

**Table 2: Structure and property of $Sb_2Se_3$ compound [17]**

| | |
|---|---|
| **Energy band gap** | **1 - 1.5 eV** |
| **Structure** | **Orthorhombic** |
| **Lattice parameters** | **a=11.62Å, b=11.77Å, c=3.962Å** |
| **Absorption coefficient** | **$>10^5$/cm** |
| **Thermal conductivity** | **Low (<10W/ (m k))** |
| **Electrical conductivity** | **High ($10^{-6}$-$10^{-5}$ S/cm)** |

# CHAPTER 2: LITERATURE REVIEW

## 2.1. Experimental Research

Razykov *et al.* [18] prepared $Sb_2Se_3$ by chemical molecular beam deposition by using polycrystalline $Sb_2Se_3$ with stoichiometric composition as source material. The Borosilicate glasses were used as substrate and the substrate temperature was varied within the range of 743-863 ºC. During the deposition, hydrogen gas was flown through the chamber. The thin film characteristics were investigated through XRD, EDS, SEM and Hall effect measurement apparatus. The thickness of the film is measured to be 2 μm by micro-interferometer. In XRD, the peak (2 2 1) is found out to be more prominent. It was observed that the structure is more affected by the flow of hydrogen during the deposition. Low hydrogen flow led to Se-rich samples and high hydrogen flow led to Sb-rich samples. The band gap was found out to be 1.2 eV with high absorption coefficient $10^5$ $cm^{-1}$. The conductivity was found to be *p*-type. This sample's results favoured to be used as an absorber layer for solar cells.

Kondrotas *et al.* [19] prepared $Sb_2Se_3$ by vapour transport deposition. The growth process was done with Mo, CdS, ZnO, $TiO_2$ substrates and the source and substrate temperature were varied for various growth conditions. The source temperature was varied within 470-550 ºC. The size of grain increased as the substrate temperature increased and when substrate temperature exceeds 290 ºC at fixed source temperature (510 ºC), film did not stick to the surface. Film thickness was observed to be increasing after substrate temperature due to change in orientation and grain size. It was witnessed that the substrate having (h k 1) orientation leads to higher growth rate and the orientation (h k 0) led to slow growth rate of grain. This proposed growth model provides different growth regime at different source and substrate temperature.

Tiwari *et al.* [20] prepared $Sb_2Se_3$ by electron-beam evaporation method. The bulk $Sb_2Se_3$ was synthesized by mechanical alloying through ball milling, with stoichiometric ratio of Sb and Se precursor as 2:3. At substrate temperature 100 ºC, the thin films were prepared at a fixed voltage ~5 kV and electron-beam current 30 mA. The soda lime glass was used as the substrate. The sample was investigated through XRD, Raman, SEM, EDS

and Optical characterization. From XRD, the diffuse pattern was observed, due to low substrate temperature. The maximum intensity peak was found of (2 2 1) orientation. SEM and EDS yield the atomic percentage of the sample, that turned out to be Sb-rich. From optical studies the band gap was determined as 1.26 eV.

Kumar *et al*. [21] prepared $Sb_2Se_3$ by thermal evaporation method at low temperature. The solar cell was configurated as Glass/ITO/ZnO/CdS/Sb2Se3/Au. $Sb_2Se_3$ was deposited on Glass/ITO/ZnO/CdS at substrate temperature 300 ºC by keeping the source in a graphite crucible at 700-800 ºC and rate at 0.28 nm/sec. Some of the samples were annealed at 300º C and 350º C. In XRD measurement for all samples, (2 2 1) (1 4 1), (0 4 1) and (0 6 1) were observed peaks but in samples annealed at 350º C, peaks at (2 2 0) and (0 4 0) were observed. In (h k 1), the grain orientations were vertical on substrate where in (h k 0) it was horizontal. Raman characterization also favoured XRD. Post deposition, the Raman bands exhibited frequency shifts to higher values. Cu is added at the top layer of $Sb_2Se_3$ which enhances the productivity. The stability is found out to be 35% with light soaking effect even at 80 ºC.

Ghosh *et al*. [22] used ultra-high vacuum molecular beam evaporation technique to prepare $Sb_2Se_3$. Lime-glass is used as the substrate. This method promises minimal fluctuations and control in deposition rate and independent control of substrate temperature. The pressure was maintained at $10^{-7}$ torr. They varied the substrate temperature as 410 ºC, 459 ºC, 550 ºC and 600 ºC. From SEM analysis of the sample deposited at substrate temperature of 410 ºC, few grains were observed (may be due to the insufficient kinetic energy of $Sb_2Se_3$ molecules) but on increasing temperature the grains were visible up to size ~ 50 nm. Elemental analysis revealed that at lower substrate temperatures a strong Si peak was observed. EDS measurements indicated a small loss in Se in higher substrate temperatures. From XRD study it showed the nanocrystalline nature of the sample. The crystallite size increased as the evaporation temperature increased. Raman showed a blue shift which might lead to possibility of presence of slight strain. From optical studies it was observed that the bandgap gets narrower as the evaporation temperature increased.

## 2.1. Computational research

Mamta *et al.* [23] proposed a solar cell with $Sb_2Se_3$ as absorber layer by simulation using SCAPS-1D software. The aim was to focus on behavior of solar cell with changing parameters. The structure was Mo/$Sb_2Se_3$/ ZnS/ZnO/front contact. $Sb_2Se_3$ and ZnS has a bandgap of 1.2 eV and 3.68 eV, respectively. A work function of greater than 4.8 eV for back contact was preferable for operation of solar cell. The thickness of ZnO, ZnS and $Sb_2Se_3$ were 0.15 μm, 0.05 μm and 1.00 μm respectively. The operating temperature was 300 K, keeping incident light at 1000 $W/m^2$. The conclusion indicates that when the thickness surpasses the optimal value, the probability of recombination rises. For 1 μm thickness the maximum efficiency was found out to be 24.76 %. The results indicated work function of back contacts to be higher than 4.8 eV to enhance back energy band alignment.

Lin *et al.* [24] prepared the structure Au/ $Sb_2Se_3$/CdS/FTO and simulated through SCAPS-1D software and calculated the performance parameters. The work function of back and front contact were 5.1 eV (Au) and 4.4 eV (FTO), respectively. The working temperature was kept 300 K and the light was projected from the side of FTO by the standard AM1.5 spectrum. The thickness of $Sb_2Se_3$ and CdS were kept as 390 nm and 60 nm. The configuration resulted a short-circuit current density of 38.15 $mA/cm^2$, an open circuit voltage of 0.408 V, a fill factor of 74.08% and a power conversion efficiency of 11.52%. After optimization of various parameters 16.5 % efficiency was obtained.

# CHAPTER 3: EXPERIMENTAL WORK

## 3.1 Thin film deposition by Electron beam evaporation method

Among the wide range of technologies electron-beam evaporation is one of the precise and versatile technique. It is a PVD (Physical vapor deposition) process which includes emission of electron from the electron gun to hit the target material. The material gets vaporized and get condensed on the substrate and a uniform thin layer is formed. The advantage of the electron beam evaporation is, the direct heating of the target, high temperature at the point of contact and precise control. This process is performed in high vacuum (~$10^{-6}$ mbar) to avoid contamination and to yield high quality pure precursors [25].

### 3.1.1 Vacuum Coating Unit

A vacuum provides a clean environment devoid of possible contamination from other gases present in that environment. Vacuum is required to get rid from the confounding air particles. It helps to remove collision by increasing mean free path between molecules and eliminate thermal convections and control deposition of atomic species [26].

**Table 3: Classification of Vacuum**

| Vacuum | Pressure (torr) | Number density ($m^{-3}$) | Mean free path(m) |
|---|---|---|---|
| Atmosphere | 760 | $10^{25}$ | $10^{-8}$ |
| Rough | $10^{-3}$ | $10^{19}$ | 0.05 |
| High | $10^{-6}$ | $10^{16}$ | 50 |
| Very high | $10^{-9}$ | $10^{13}$ | $10^{3}$ |
| Ultrahigh | $10^{-12}$ | $10^{10}$ | $10^{6}$ |

There are several methods available to create vacuum by using different pumps like Mechanical Oil sealed pump, Mechanical, Turbomolecular pump, Roots pump, Vapor booster pumps etc. Mechanical oil sealed pumps are capable to achieve pressure to $10^{-2}$ mbar. Vapor pumps are used to achieve pressure up to $10^{-6}$ mbar. Oil sealed pumps are classified to rotary vane type and sliding vane type. To measure the vacuum several gauges (Pirani gauge, penning gauge, Mcleod gauge) are used [26].

### 3.1.1.1 Rotary pump and diffusion pump

### 1. The Rotary Vane type oil sealed pump

The stator is a hollow cylinder, which has an inlet port connected to the system and an outlet port covered by a valve. The rotor is a steel cylinder having a shaft mounted in, whose axes are similar to the stator. The vanes are steel plates with rounded ends making contact with the wall of rotor. The line of contact between rotor and stator wall is called *top seal*. This whole assembly is submerged inside a suitable oil [27].

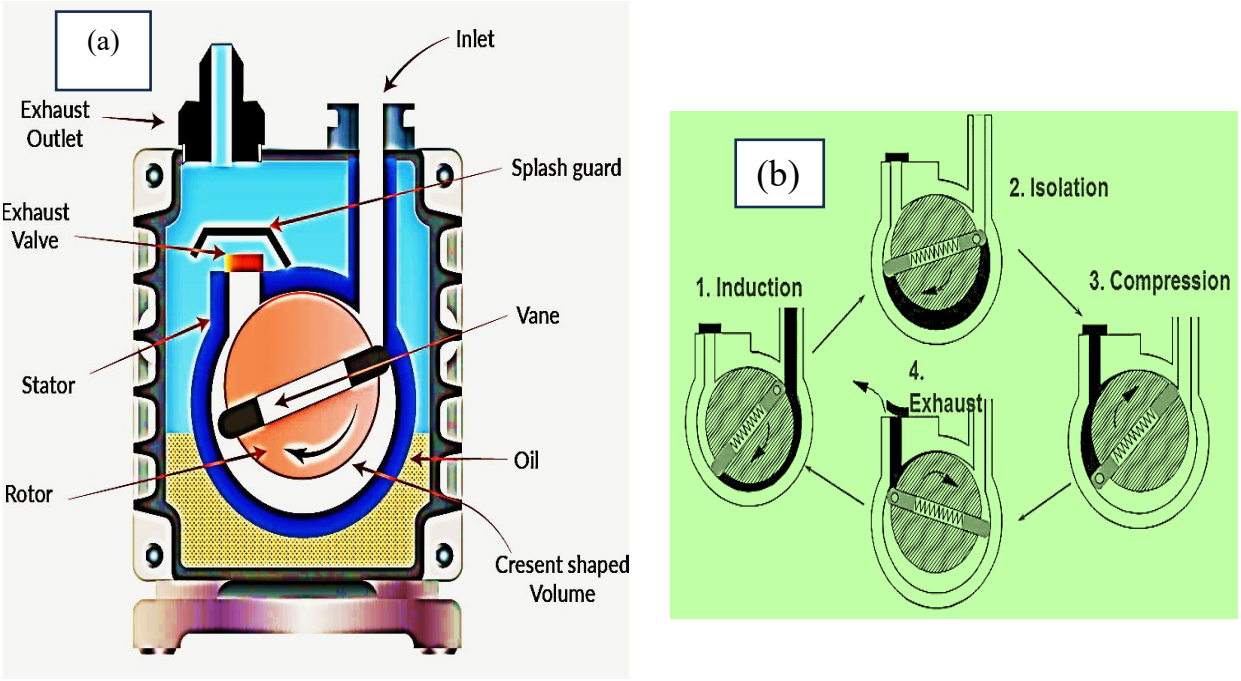


**Figure 13(a): Schematic diagram of Rotary pump, (b): Mechanism of Rotary pump**

Rotary pump works on the mechanism of Boyle's *law.* As per the figure 12(b) at first stage when the vane sweeps out, the volume increases and pressure decreases and this continues till the end of vane crosses the inlet port. This is the induction stage.

Then isolation of this gas remains until the vane approaches the top seal. In this isolation stage the volume reduces and the pressure increases and compression occurs. when it approaches the exhaust port the pressure is enough to let the gas out of the system. The oil provides lubrication, sealing and high compression ratios at low inlet pressure. The optimum pressure can be obtained by this pump is $10^{-3}$ mbar [27].

2. **Diffusion Pump**

Diffusion pump, also known as vapor diffusion pump, is a non-mechanical pump acting upon the principle of momentum transfer mechanism.

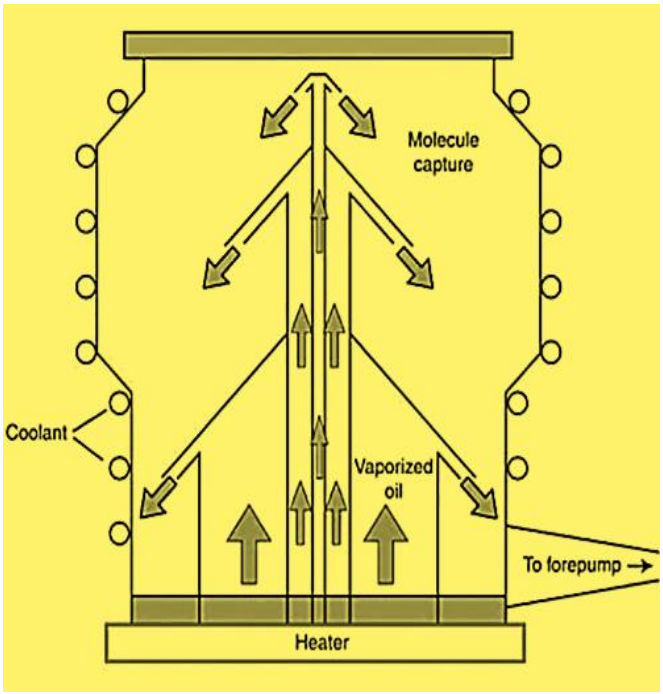


**Figure 14: Mechanism of diffusion pump**

Diffusion pump comprises of a cylindrical body attached with a heater at base and surrounded by coolant for the cooling purpose of the body while heating. The chimney (jet) with umbrella structure is mounted on the boiler. The heater consists of an oil, which turns into vapor and travel through the chimney and deflection occurs by the umbrella, which makes the stream go downwards with high speed. Gas molecules in vapor stream suffer downward momentum due to collision and get exhausted. The vapor condenses to liquid due to interaction with coolant and comes back to the boiler. To get higher pumping

speed, the area between jet and the pump wall (admittance area) has to be more, which may lead to back-diffusion. Back-diffusion is when vapor molecules lose its momentum due to more collisions. To achieve high pumping speed, instead of single jet structure multiple jet design is introduced. They act as backing pumps to one another. The upper jets have higher admittance area and high pumping speed and lower ones have less admittance area and hence denser vapor streams. The pressure difference is generated inside the pump. The vacuum becomes high (~$5\times10^{-5}$ mbar) at lower jet areas and low (~$5\times10^{-1}$ mbar) at upper jet areas [27].

### 3.1.1.2 Pirani Gauge and Penning Gauge

#### 1.Pirani Gauge

It is a low-pressure gauge operating to measure vacuum in the high to medium range. It acts upon the principle of dependence of thermal conductivity with pressure, also known as thermal conductivity gauge. At low pressure, thermal conductivity is expected to vary linearly with pressure. Consider a metal filament getting heated by electric current. At high pressure, the intermolecular collision causes heat transfer and heat loss, which is independent of pressure but as the pressure falls, molecule-wall collision dominates and heat loss depends on the pressure directly and starts to fall which yields rise in the temperature and so in resistance. It demonstrates a new relation between electrical resistance and pressure [26].

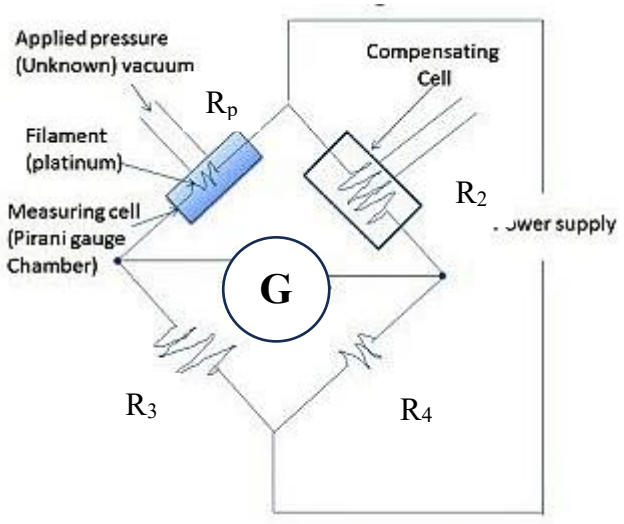


**Figure 15: Working mechanism of Pirani gauge**

To measure the resistance, the typical method of Wheatstone bridge is used. The filaments are made up of platinum. As per the figure 14, one of the resistances is exposed to the chamber and to record, a galvanometer is connected. When the power supply is on, current flows through the filament. When the pressure changes, variation in temperature occurs which leads to rise or fall in resistance. Galvanometer is used to detect it and it can be easily converted in terms of change in pressure. On the opposite side, there is a compensating cell which helps to avoid effect of external environmental pressure [27].

From the figure,

$$\frac{R_p}{R_2} = \frac{R_3}{R_4} \qquad \text{..... (7)}$$

Where $R_p$= resistance of the filament connected to the chamber

$R_2$= compensating resistance (adjustable)

$R_3$, $R_4$= fixed resistances

**2.Penning Gauge**

It is an ionization gauge used to measure vacuum in high range. It acts based on the principle of ionization of gas molecules. The number of ions produced is directly proportional to the molecular density and hence to the pressure inside the chamber [27].

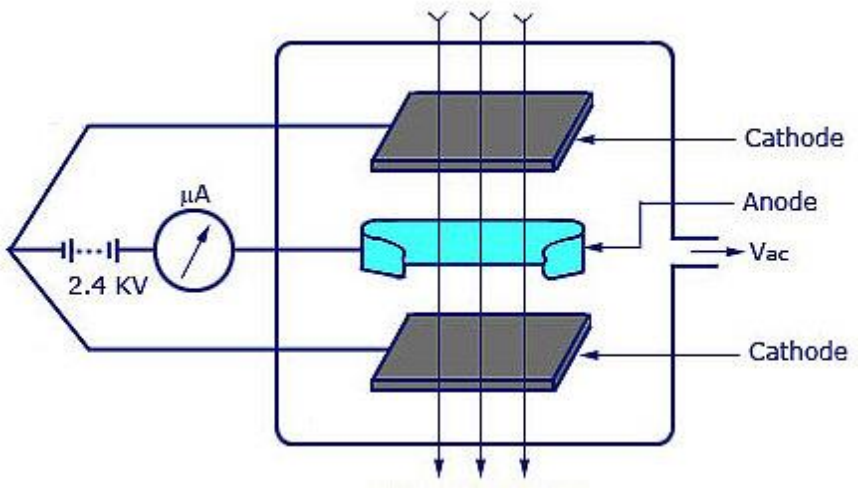


**Figure 16: Penning gauge working principle**

The cathodes are placed parallelly and anode is placed in between them as per the figure 15. A magnetic field (~400 gauss) is applied perpendicular to the plates. A potential difference of 2-4 kV is applied between anode and cathodes. Assuming an electron near a cathode plate travelling towards anode in influence of electric field in a helical path (effect of magnetic field) and then coiled back due to another electric field caused by another cathode. The electron keeps on oscillating in a loop. Due to the electric field, electron gets enough kinetic energy to ionize a gas molecule it collides. The secondary electron can ionize the gas molecule too which leads to rise the ionization. Eventually the electron gets captured by anode and the positive ions by cathode which yields current to be measured. The more the gas molecules, more the ionization and it is directly proportional to current. The pressure can be measured from this current by calibration. There is a difficulty to build-up an ionization at low pressure, insufficient to initiate the process. At pressure ~$10^{-2}$ mbar the process of ionization can be started easily [27].

### 3.1.2. Quartz Thickness Monitor (QTM)

Quartz thickness monitor, also known as Quartz microbalance monitor is a device which measures the thickness deposited on the substrate i.e. the thickness of thin film. It establishes a relation between mass and frequency. The mass deposited on the surface of quartz crystal affects the frequency of it. It works on piezoelectric effect [28].

**(a)** **(b)**

**Figure 17(a): Quartz crystal monitor outside view; (b): Quartz crystal monitor inside view**

Quartz is a piezoelectric material. When a high frequency AC voltage regulates at resonance frequency the amplitude of vibration is maximum. The resonance frequency

varies with film deposition. By measuring the change in frequency, the film thickness can be measured.

$$\Delta f \longrightarrow \Delta m$$

where, $\Delta f$ = frequecny change of quartz crystal monitor

$\Delta m$ = change in thickness due to deposition

**Tooling factor**

Tooling factor is a necessary measurement in electron beam deposition.

$$\text{Tooling factor} = \frac{(Distance\ from\ crucible\ to\ QCM)^2}{(Distance\ from\ crucible\ to\ substrate\ holder)^2} \times 100$$

The tooling factor was calculated to be 78.88.

### 3.1.3. Other elements of electron beam system

**1. Electron source:** Electron gun consists tungsten filament which produces high energy electron when a high potential difference is applied across it. To generate the electron beam and to control, a separate system is employed through which we can get control over the electron beam intensity. The deposition rate can be controlled by reducing or rising the electron density. In the experimental work we apply 5.2 kV voltage across the filament and vary the current density according to the element to be deposited.

**2. Magnetic alignment:** This alignment is introduced to direct the electron beam to the target element inside the crucible. The magnets create a uniform magnetic field in a localized region only, which is perpendicular to the path of electron beam. Here the magnetic field caused by the magnets bends the electron 180º from the original direction.

**3. Crucible:** It is supposed to carry the target material inside the chamber. It should be a non-reactive material to avoid unnecessary reactions and of high melting point like molybdenum or graphite. Here the system comprises of 4 crucibles, which position can be changed respectively [25].

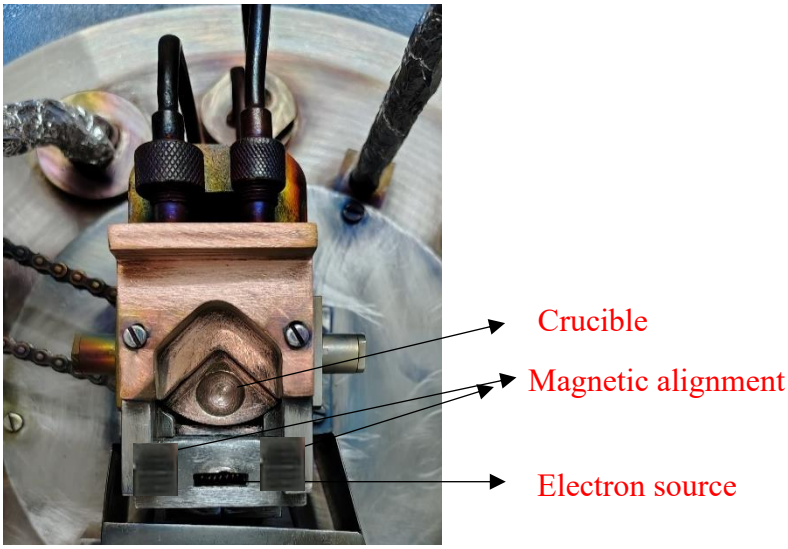


**Figure 18: Crucible, Electron gun and magnets inside the chamber**

## 3.2. Fabrication of $Sb_2Se_3$ thin films

### 3.2.1. Substrate Preparation

In the deposition of $Sb_2Se_3$ thin film we have used Soda-lime glass as the substrate. The glass has dimension of 76 mm × 26 mm × 1mm. The substrate with no scratches, no stain and no defects were selected and washed with soap and water properly. After cleaning it was rinsed with deionized water and dipped in it for few minutes. Then the substrate was subjected to ultrasonic cleaning with deionized water twice. This process ensures the cleaning of surface and removes the residues by its vibration. Deionized water is used to avoid any mineral build up as it has no ions or mineral. Then the substrate was cleaned with boiling ethanol. After the cleaning of substrate, it was loaded on the substrate holder followed by dry cleaning. A substrate holder has space for 3 substrates at once. The material to be deposited were Cu, Sb, and Se, which were loaded on the crucible. These have 5N purity. The whole arrangement is enclosed by a bell jar

**Figure 19: Ultra sonication of glass substrate**

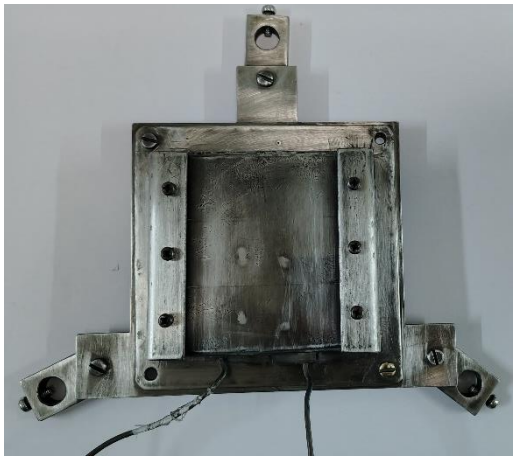

**Figure 20: Substrate holder**

### 3.2.2. Vacuum generation and deposition

The arrangement of deposition is surrounded by a bell jar inside which the vacuum is created. The bell jar is assisted with a gasket beneath it which supports vacuum generation. Rotary pump is used to create vacuum inside the chamber up to $10^{-2}$ mbar. Roughing valve and backing valve are opened to create low range vacuum. Pirani gauge is used to measure the pressure as it is a low-pressure gauge. Diffusion pump is used to generate pressure of $10^{-6}$ mbar. Penning gauge is used to measure the high vacuum range. This pressure is kept constant throughout the process. The substrate is heated up to 100 ºC and this temperature is maintained across the deposition. The density, acoustic impedance and tooling factor are put into Digital thickness monitor which shows the rate of deposition and the thickness deposited during the process of deposition [27].

**Figure 21: Electron beam evaporation method set up**

### 3.2.3. Stack Variation and Film composition

Antimony (Sb) and selenium (Se) were deposited in stack elemental layers. As the sticking coefficient of Sb is low there may be some difficulties in sticking of Sb with glass substrate. Copper has high sticking coefficient [29]. A thin layer of copper with composition 0f 1% was deposited first on the glass substrate and also on the top of the layers. The stack order was Cu/$Sb_2Se_5$/Cu as shown in figure 23. There might be chances of evaporation of selenium, to compensate the selenium loss we deposited $Sb_2Se_5$.

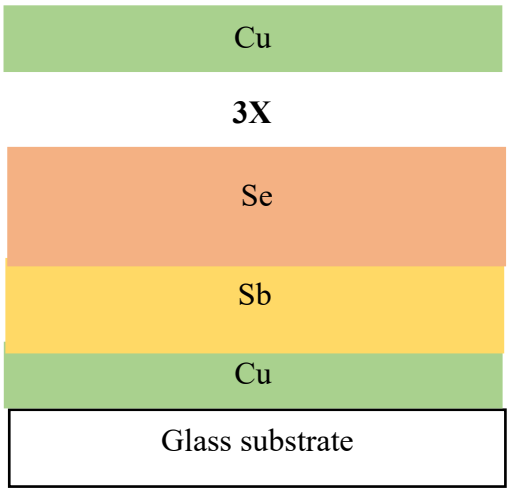


**Figure 22: Stacking order of precursor film**

**Table 4: Thickness and rate of deposition of Cu/$Sb_2Se_5$/Cu precursor thin film**

| Elements | Thickness to be deposited | Rate |
|---|---|---|
| Cu | 40 Å | 0.3-0.4 Å/s |
| Sb | 1240 Å | 1.5-2.5 Å/s |
| Se | 2760 Å | 2.5-3.5 Å/s |
| Total thickness to be deposited | ~0.4 $\mu$m | |

**Figure 23: Cu/$Sb_2Se_5$/Cu thin film precursors deposited by e- beam**

## 3.3. Annealing of precursor films

Annealing is a process in which thin layers typically deposited on a substrate are heated to a particular temperature and let to cool down in a regulated manner. This heating and cooling process improves the grain growth, crystallization, stability, electrical and optical characteristics etc.

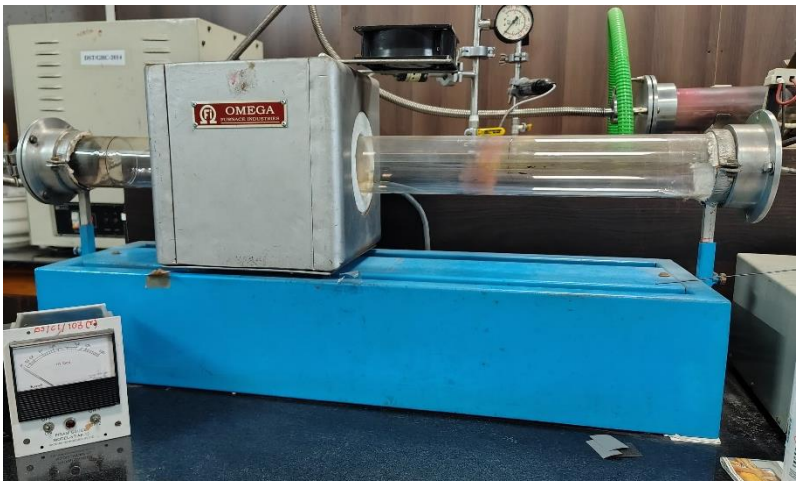


**Figure 24: Horizontal Tubular Furnace**

To anneal the thin film precursors, we take small precursors of 1 cm × 1cm dimension and they are closed inside the graphite box, covered with copper plate. The process is carried out inside the horizontal tubular furnace. Evacuation of quartz tube is carried out up to $10^{-2}$mbar using rotary pump. The argon gas is passed through the tube which carries the impurities with itself. Once the evacuation is properly done, the heating is performed at a specific temperature in argon environment followed by cooling. Table 5 shows the different annealing conditions. To compensate for loss of selenium, we performed selenization of precursors with 30 mg of selenium powder. Beyond the temperature of 225 ºC, the samples were getting peeled off. After selenization, the precursors were soft annealed too at maximum temperature of 225 degrees. All these processes were carried out at 600 mbar argon gas pressure.

**Figure 25: Graphite box with Graphite plate**

**Table 5: Cu/$Sb_2Se_5$/Cu thin films annealed at different parameters**

| Sample | Amount of Selenium | Temperature of Annealing | Time of Annealing | Pressure |
|---|---|---|---|---|
| 1 | 30 mg | 200 ºC | 15 min | 600 mbar |
| 2 | 30 mg | 225 ºC | 15 min | 600 mbar |
| 3 | 0 mg | 225 ºC | 15 min | 600 mbar |

## 3.4 Characterization Methods

### 3.4.1 X-ray Diffraction method

X-ray diffraction method is one of the characterization techniques used in laboratory to analyze structural information like chemical composition, crystal structure, crystal orientation, lattice strain etc. The X-ray from the source gets scattered with atoms arranged in a crystal due to its small wavelength, gives a unique pattern. This pattern is considered as fingerprint of a material [30].

**Bragg's Law:**

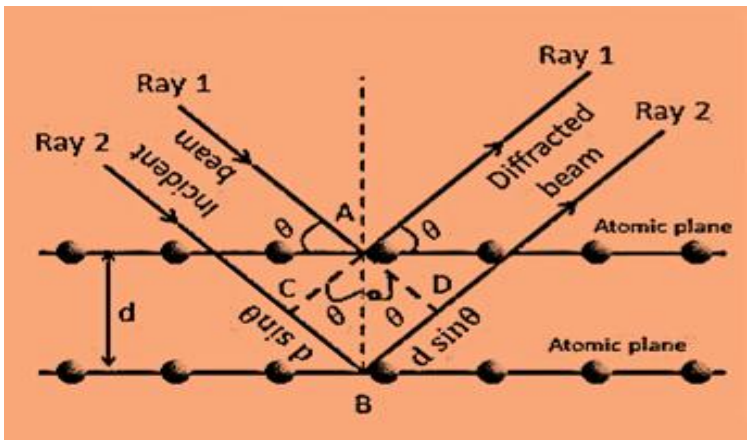


**Figure 26: X-ray diffraction by lattice surface**

Considering a monochromatic X-ray of wavelength $\lambda$ falling at angle $\theta$ on the crystal of periodic arrangement. The interplanar spacing is *d*. Let the x-ray is incidented at point $A_1$ at angle $\theta$ and gets scattered at same angle. Incident beams Ray-1and Ray-2 get scattered at point A and B respectively at angle $\theta$.Let AC and AD are the perpendiculars from A to both incident and diffracted ray of Ray-2 respectively. The path difference of

Ray-2 is greater than Ray-1 by factor CB+BD. For a constructive interference the path difference is n$\lambda$.

$$\therefore \ \boldsymbol{\lambda = 2d\sin\theta} \qquad \ldots. (7)$$

If (hkl) are the miller indices of a plane then ula we may find (hkl) by using value of d and lattice parameters (a, b, c) [31].

$$\mathbf{d} = \frac{\mathbf{1}}{\sqrt{\frac{\mathbf{h^2}}{\mathbf{a^2}} + \frac{\mathbf{k^2}}{\mathbf{b^2}} + \frac{\mathbf{l^2}}{\mathbf{c^2}}}} \qquad \ldots. (8)$$

### 3.4.1.2 Debye-Scherrer's formula

The crystallite size can be calculated by using Debye-Scherrer's formula.

$$\mathbf{D} = \frac{\mathbf{k\lambda}}{\boldsymbol{\beta}\mathbf{\cos\theta}} \qquad \ldots. (9)$$

Where D = Crystallite size

$\lambda$ = Wavelength of incident X-ray

$\beta$ = Full width at half maximum (in radians)

k = Scherrer's constant

### 3.4.1.3 X-ray Diffractometer

**X-ray source:** It contains electron source, metal target and accelerating potential. When accelerated high energetic electron collides with metal target X-rays are generated. In general Cu and Mo characteristic spectrums are used as X-rays.

**X-ray diffraction method:** Powder method and Oscillation method are used as methods to diffract X-rays.

**Detection of X-ray source:** Photographic films, Geiger counter, Proportional counters are used to detect diffraction pattern of X-rays [30].

**Figure 27**: **X-ray diffractometer**

### 3.4.2 Raman Spectroscopy

Raman Spectroscopy is a powerful technique used to analyze the vibrational, rotational and other frequency modes of vibrations in a sample. This can be considered as the helping hand of XRD as it goes in accordance with the XRD data. In this method we project laser light to sample and study the change in energy of light when it interacts with the vibrations of the sample. It is non-destructive, versatile, highly specific and reliable. When light gets absorbed by the sample the electron goes to higher state and then releases energy, which can be classified into 3 types. If there is no change between the frequency of light emitted and the frequency of light absorbed then the line is called Rayleigh line. If the frequency of emission exceeds slightly then it is Anti-stoke line and if the frequency reduces slightly it is Stoke-line. The necessary condition for the sample to be characterized under Raman Spectroscopy is to have polarizability [30].

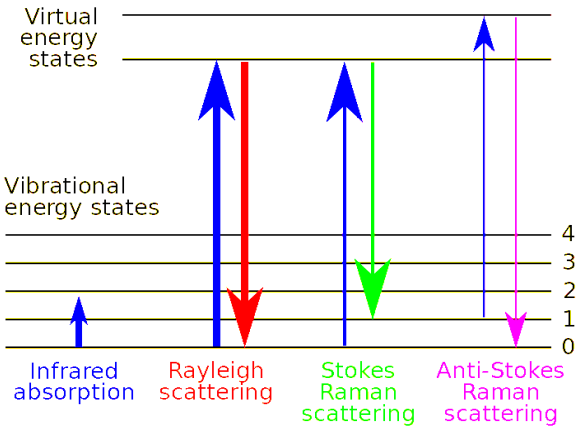


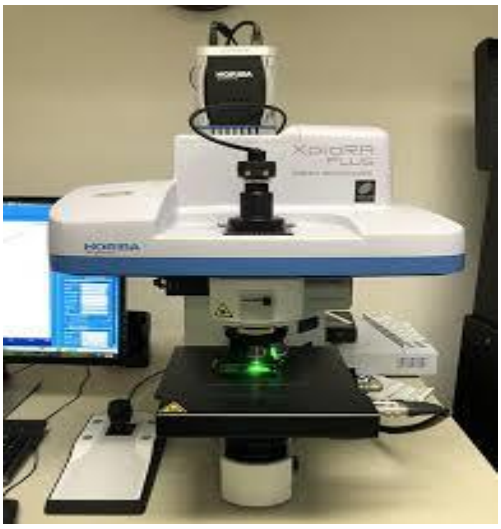

**Figure 28**: **Various vibrational states**

**Figure 29: Raman Spectroscopy**

The Raman Spectroscopy apparatus consists of an excitation laser, which excites the electron to higher energy. Monochromatic lasers are generally used. Light is divided by a beam splitter and then one path is projected on sample and another is focused through lens, then passed through notch filter and goes to spectrometer. The filters are used to select a particular wavelength range. There are photomultiplier tubes as detector to collect the emitted photons of particular frequency [30].

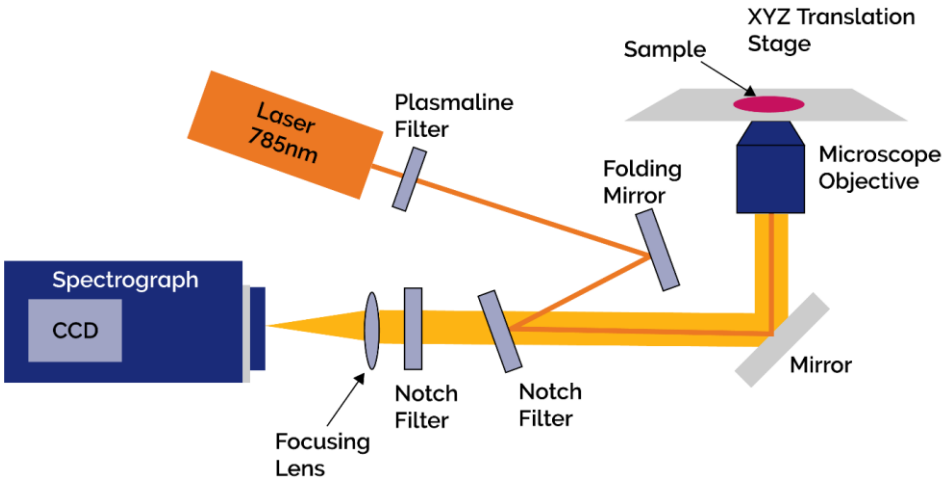


**Figure 30: Schematic of Raman Spectroscopy**

### 3.4.2 UV-Visible-NIR Spectroscopy

UV-Visible-NIR spectroscopy is an analytical technique that covers a broad range from ultraviolet to visible and near infrared used to determine optical properties of liquids and solids. It provides lights from lower to higher wavelength to analyze Transmittance, Reflectance, Absorbance of a material. Optical absorption is the principle of this characterization techniques. Absorption of photons depends upon the intensity of the incident photon flux [32].

The set up comprises of a light source, a monochromator and a detector. The light from monochromator splits into two paths, pass through reference and sample. Both are detected by a photodetector.

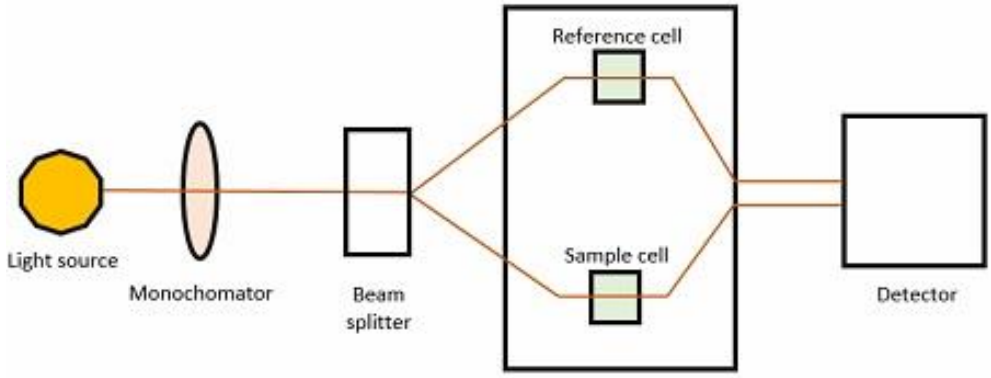


**Figure 31: Schematic diagram of double beam spectrophotometer**

The principle of double beam spectrophotometer works on Beer Lambert's law. It states that when the light is passed through an absorbing medium, the rate of intensity is directly proportional to the concentration and path length.

$$\mathbf{I = I_0 e^{-\varepsilon c L}} \qquad \text{..... (10)}$$

Where c= molar concentration

L= thickness

$\varepsilon$ = molar extinction coefficient

The band gap is calculated using reflectance spectra. The Kubelka-Munk function is used to measure the band gap of the sample. The theory of P. Kubelka and F. Munk helps in transformation of reflectance spectra to absorbance spectra.

$$\mathbf{F(r) = \frac{k}{s} = \frac{(1-R)^2}{2R}} \qquad \text{.... (11)}$$

**Figure 32: UV-Visible-NIR Spectroscopy apparatus**

### 3.4.3 Hall effect measurement system

Hall effect is the generation of potential difference across a semiconductor or conductor transverse to the electric applied to it and perpendicular to the magnetic field applied. The potential difference is called Hall voltage [33].

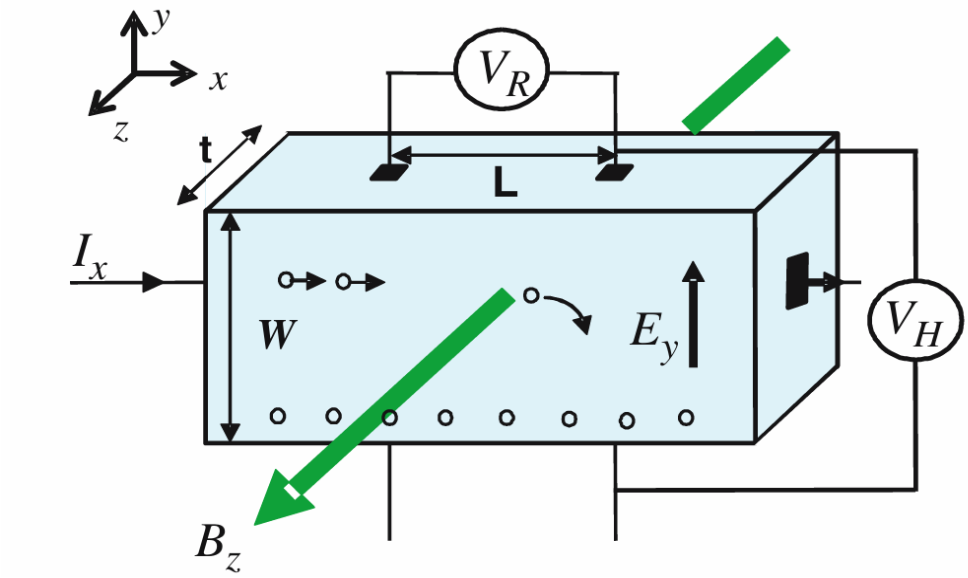


**Figure 33**: **Representation of hall effect in a p-type semiconductor**

Hall effect is used to measure charge carrier mobility, carrier polarity, carrier density. The resistivity of the sample depends upon the carrier density and carrier mobility.

We can measure resistivity and conductivity of a specimen by hall effect measurement. Let the magnetic field($B$) is $z$ direction and current($I$) in $x$ direction. As per the figure due to Lorentz force some charge carriers diverge from the current direction leads to formation of voltage drop $V_H$ across $y$ direction [33].

Lorentz force indued on a charge the transverse magnetic field is

$$\mathbf{F_L = q(v \times B) = -qv_xB_z} \qquad \text{…….. (12)}$$

Where $v_x$ is the velocity in x direction.

Due to this there is an electric field arises in $y$ direction which rises an electronic force $F_{EL}$. The Lorentz force is balanced by the force $F_{EL}$.

$$\mathbf{-qv_xB_z + qE_y = 0} \qquad \text{……. (13)}$$

By interpreting formula for $v_x$ we may determine hall voltage as,

$$\mathbf{V_H = \frac{BI}{qtp}} \qquad \text{……. (14)}$$

Where B= magnetic field applied

I= applied current

t= conducting layer thickness

p= carrier density in p-type

As t is known to us the hole concentration can be calculated as function of hall co efficient $R_H$ as followed.

$$\mathbf{R_H = \pm \frac{tV_H}{BI}} \qquad \text{……. (15)}$$

Where $$\mathbf{p = \pm \frac{1}{qR_H}} \qquad \text{. …… (16)}$$

(+ sign indicates the material is p-type and – sign indicates the material to be n-type)

To determine mobility ($\mu$),

$$\boldsymbol{\mu = \frac{|R_H|}{\rho}} \qquad \text{…… (17)}$$

Where $\rho$ is the resistivity of the material.

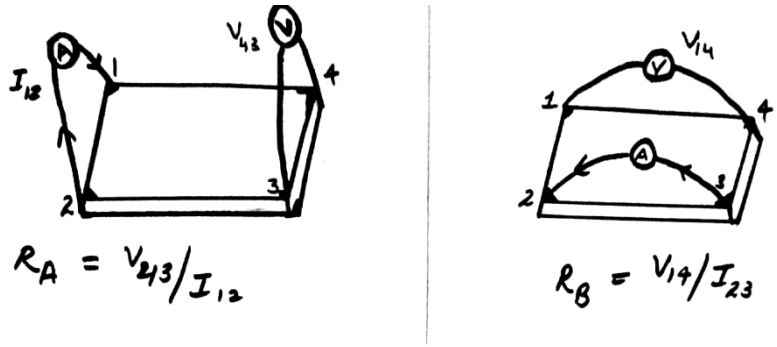


**Figure 34: Current and voltage presentation in Hall effect**

Apart from hall voltage set up resistivity also ca be determined by Vander paw method.

In this method resistivity can be determined precisely and effectively for small dimensions too. The contacts with less dimension than the sample are to be placed at the perimeter of the sample with uniform thickness [33].

### 3.4.4. Scanning Electron Microscopy (SEM) and Energy Dispersive Spectroscopy (EDS)

Scanning electron microscopy and Energy Dispersive Spectroscopy are powerful characterization tools used to scan the surface structure of a specimen by using high-energy focused electron beam. The beam interacts with the specimen and generates various signals like secondary electrons, bac scattered electrons, X-rays and these signals combinedly get collected to yield a clear picture of surface structure and morphology of the specimen [34].

The whole system contains the electron source, electromagnetic lenses to focus the beam, the deflection system and the detectors. The electron can be emitted from the source by thermal emission (energy has to be greater than the wave function), Schottky effect (electric field is applied to reduce the work function), field emission (applied electric field is very much high).

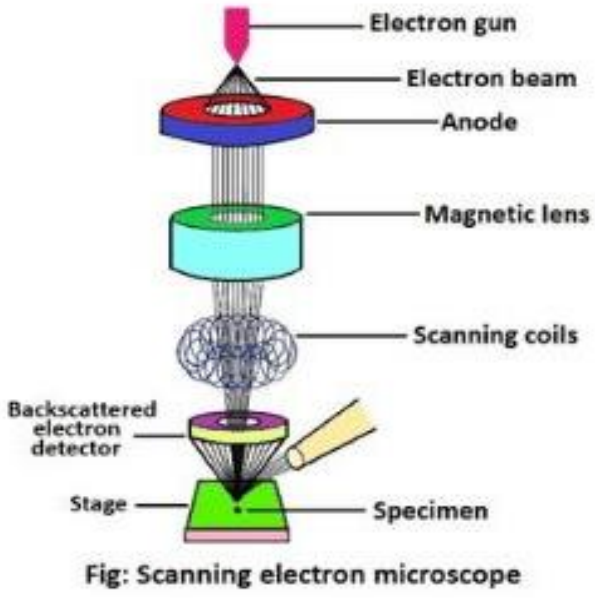


**Figure 35: Schematic diagram of Scanning electron microscope**

**SEM Analysis Procedure:**

I. A high energy electron beam of (100-30000) eV is introduced in SEM. Generally thermionic emission is used, in which electric field is applied to reduce the work function with 10 V $nm^{-1}$ field intensity, that allows electrons to depart metal by reducing potential barrier.

II. In SEM apparatus, there are lens to compress the focus of electrons on the specimen and the collected electron from final lens, penetrate the material to a depth of nearly 1 μm. There are scan coils, moving to form the picture of the material, which results in a rectangular raster on the surface. When a magnified view is needed, the coils make the beams to deflect across a tiny area.

III. The detector collects the emitted signals of electron from the scanned sample. SEM generates image of the specimen by considering both back-scattered electron and secondary electrons. In absence of detectors, the signals generated by the electron beams interaction with the surface of specimen, generates nonsensical images. Generally, on the collector surface of detector a positive voltage is applied to collect both back-scattered electron and secondary electrons and a negative voltage is applied to receive only back-scattered electrons.

IV. The operator adjusts the intensity and the brightness to enhance the clarity and the signals are displayed on the screen. Magnification above 10,000X is used when more details are needed. Using high accelerating voltage from 15 to 30 KeV, allows the reflected signals to transmit the data about interior of the sample, by penetrating beneath the surface.

V. The inclination of the sample has an impact in number of back-scattered electrons and secondary electrons. If angle of inclination is there, it increases the topographic contrast. The topography of the sample is pictured with the help of SEM which helps us to know the shape, size, grain growth and roughness of the specimen [34].

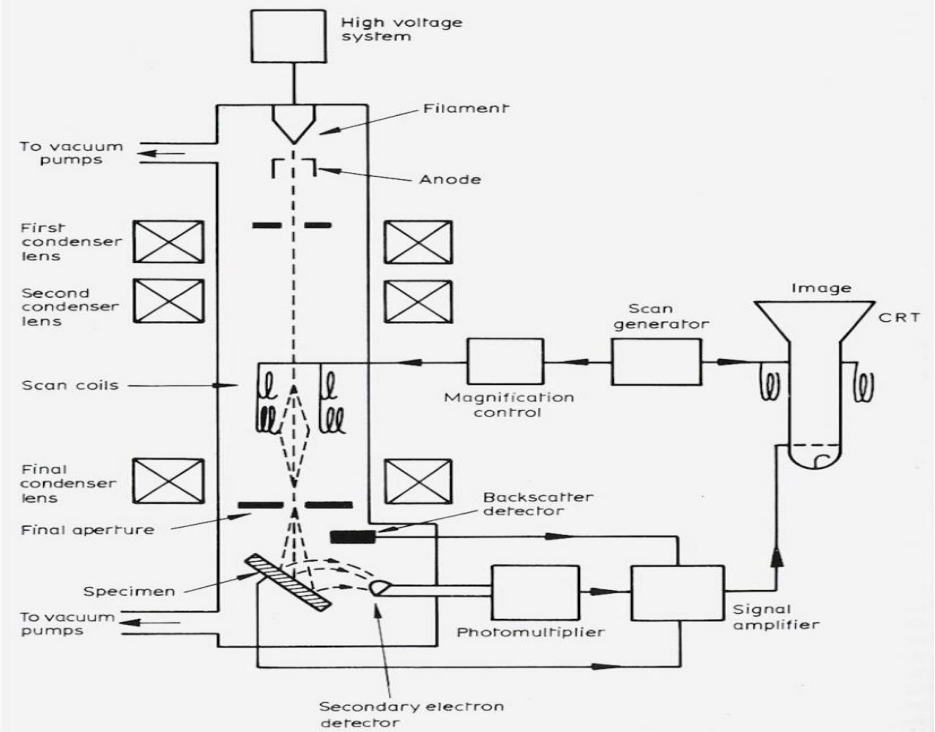


**Figure 36: Procedure of Scanning electron microscope**

**Energy Dispersive X-ray Spectroscopy**

When the sample is projected under the electron beam, there are X-rays produced due to interaction electron beam and the surface of the specimen. The electrons collide with the atom of the sample and knock out the electron from inner shell. To fill the vacancy, an electron from outer shell takes the position by releasing the extra energy. This energy is emitted as X-ray photon (characteristic X-ray). These characteristic X-rays have the energy and helps in analyzing the material [34]. There are different types of signals generated from the specimen as shown in the figure 37.

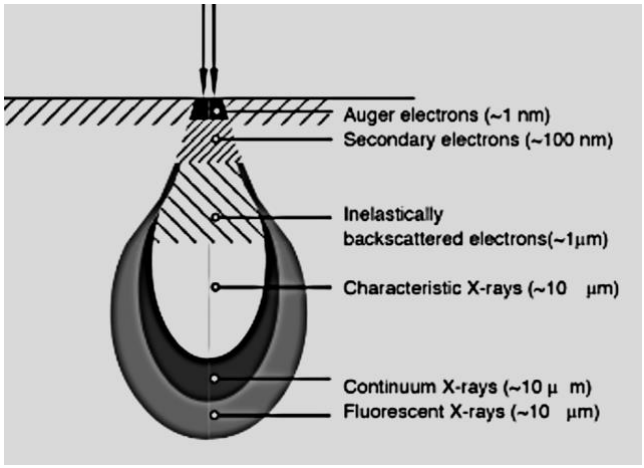


**Figure 37: Various signals generated from the specimen**

EDS detector is capable to distinguish the characteristic X-rays from various signals and it separates the energy of characteristic X-rays. A software is fixed to turn the photon energy to electrical signals and analyze the energy to determine the amplitude of various elements. Both quantitative and qualitative composition can be pictured with the help of SEM equipped EDS. The quantitative analysis is done by calculating he X-ray intensities of each element by monitoring the chemical composition. A qualitative study determine which elements are present in undertaken. At final stage the software does corrections and refine the results [34].

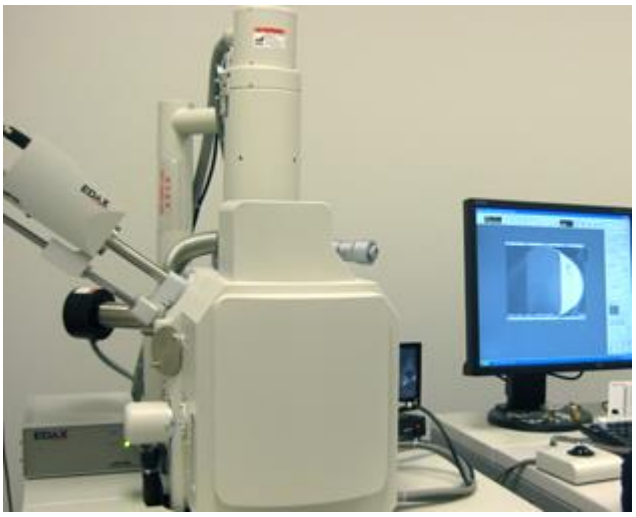

**Figure 38: SEM equipped with EDS**

### 3.4.5. Non-contact optical Profilometer

A non-contact optical profilometer is used to measure the surface topology and roughness of the sample without any physical contact, using light-based technologies to create high resolution 3D images of surface. It provides both dimensional analysis and data of surface roughness. The advantages of using this technique is, it does not changes surface characteristics and its high precision [35].

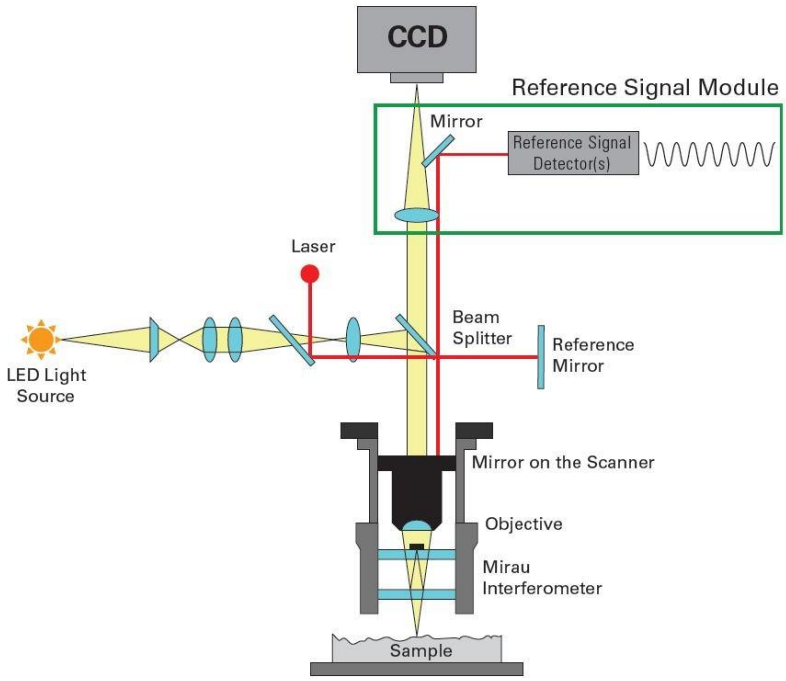


**Figure 39: Working of optical Profilometer**

The profilometer induce light on the sample working like a microscope. A beam splitter is present to divide this light into two paths. One is illuminated on a reference mirror and another is projected on the specimen. This light interacts with the surface of specimen, may be reflected, may get diffracted or scattered, depending upon surface topology. A detector is placed to detect reflections from both the lights. It collects the recombined data as recombination reduces the interference. This recombined data gives the vertical resolution on the scale of Angstroms. The optical signals are processed to give 3D image of the surface. This is a very convenient method to use in accordance with depth in understanding of surface morphology without any surface damage [35].

**Figure 40: Non-contact optical Profilometer**

Image acquisition time in an optical profilometer varies from milliseconds to several seconds, depending on the technique, resolution, and scan area. This is affected by several things like frame rates, precision, measurement technique and the kind of image we need. The term spatial resolution shows the capacity of profilometer to differentiate minute details in both dimensions [35].

# CHAPTER 4: RESULTS AND DISCUSSION

In this present work, an attempt is initiated to prepare near stoichiometric, polycrystalline $Sb_2Se_3$ thin films and study their structural, morphological, optical and electrical properties.

## 4.1. Compositional analysis

Table 6 shows the elemental composition of $Sb_2Se_3$ thin films selenized with different temperatures and selenium contents. The stochiometric ratio of Se:Sb is desired to be 3:2 [18]. The precursor annealed with 30 mg selenium powder at 225 ºC for 15 minutes at 600 mbar pressure was found to have ratio near to the desired stoichiometry. The EDS spectra of stacked layer of $Cu/Sb_2Se_5/Cu$ selenized with 30 mg selenium powder at 225 ºC for 15 minutes at 600 mbar pressure is shown in figure 41. The ratio was found to be 1.38 for the precursor annealed with 30 mg selenium at 200 ºC for 15 minutes at 600 mbar pressure. This might be due to insufficient annealing temperature. Lower temperature led to less incorporation of the selenium with antimony. For the precursor soft annealed at 225 ºC for 15 minutes at 600 mbar, the composition does not resemble with the desired stoichiometry. This might be due to selenium loss. Due to selenium evaporation, we need extra selenium to compensate for the loss of selenium from precursor. This extra selenium was not available during soft annealing.

At temperatures above 225 ºC, the sample was not stable. Hence, 225 ºC was found to be the optimum temperature. For time duration higher than 15 minutes, the samples were getting peeled off. Hence, 15 minutes was the optimum time.

**Table 6: Chemical composition of $Sb_2Se_3$ thin films annealed at different parameters**

| Annealing condition | Amount of selenium | Sb (wt.%) | Se (wt.%) | $\frac{Se}{Sb}$ |
|---|---|---|---|---|
| 225 ºC- 15min- 600 mbar | 30 mg | 40.29 | 59.71 | 1.49 |
| 200 ºC-15 min-600 mbar | 30 mg | 41.88 | 58.12 | 1.38 |
| 225 ºC- 15 min-600 mbar | 0 mg | 50.18 | 49.82 | 0.99 |

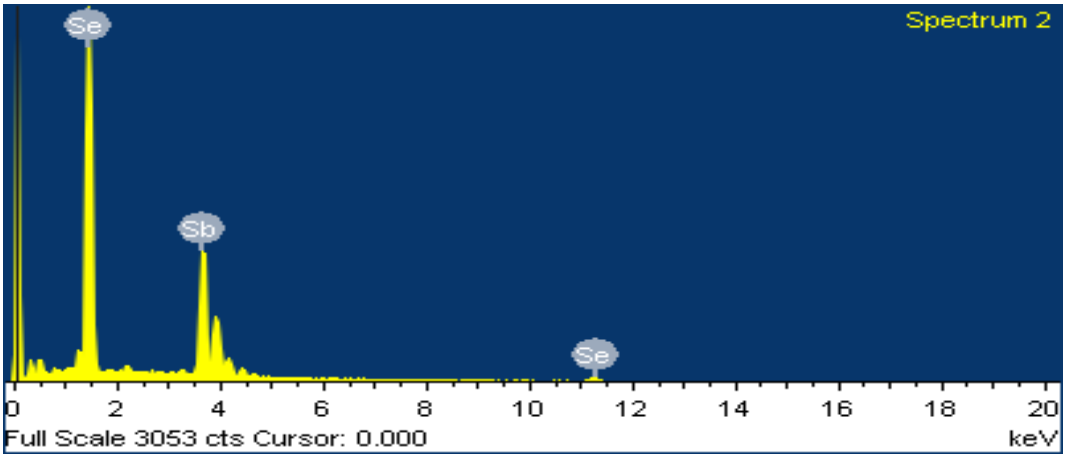


**Figure 41: EDS spectrum of Cu/$Sb_2Se_5$/Cu thin film annealed with 30 mg selenium powder at 225 ºC for 15 minutes at 600 mbar**

## 4.2. Structural analysis

### 4.2.1 XRD analysis

The XRD pattern of $Sb_2Se_3$ thin films annealed at various temperatures and with different selenium content is shown in figure 42. Single phase $Sb_2Se_3$ was observed at $2\theta$ values of 28.26º, 31.24º and 38.88º corresponding to the planes (2 1 1), (2 2 1) and (1 4 1) respectively (JCPDS 15- 0861). All the prepared thin films exhibited similar pattern irrespective of temperature and selenium content. Even at low temperature of 200 ºC, $Sb_2Se_3$ was formed.

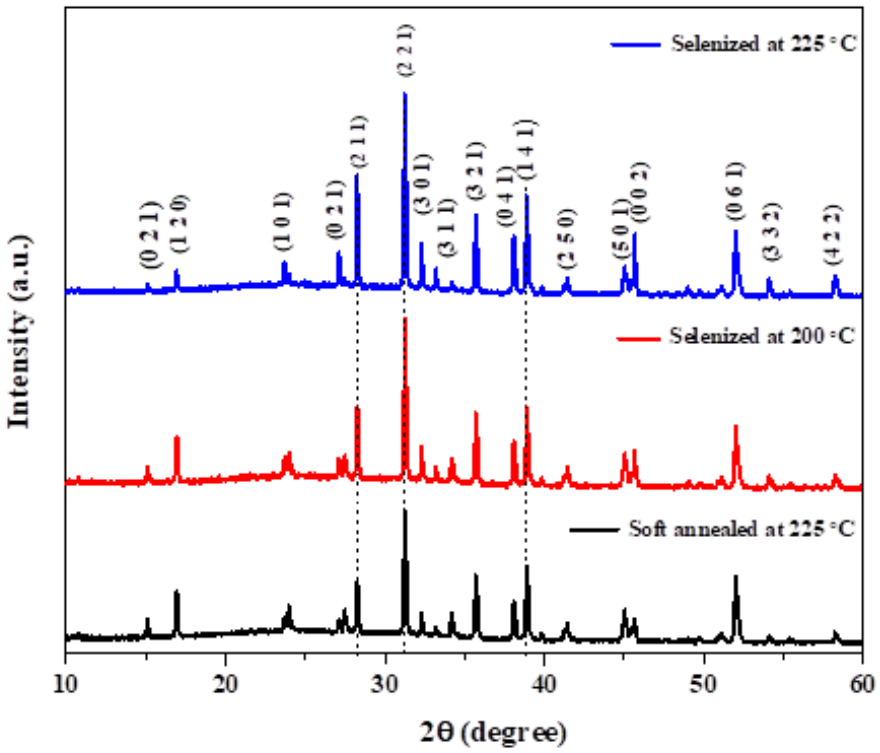


**Figure 42: XRD pattern of $Sb_2Se_3$ thin film annealed at various temperatures and with different selenium content.**

Using Debye- Scherrer's formula (from equation 9), the calculated crystalize size of the grown thin films are summarized in table 7.

**Table 7: Crystallite size of $Sb_2Se_3$ thin film annealed at various temperatures and with different selenium content**

| Annealing condition | Amount of selenium | Crystalize size |
|---|---|---|
| 225 ºC- 15min- 600 mbar | 30 mg | 76 nm |
| 200 ºC-15 min-600 mbar | 30 mg | 58 nm |
| 225 ºC- 15 min-600 mbar | 0 mg | 42 nm |

The crystallite size was found to be maximum, i.e. 76 nm, for precursor annealed at 225 ºC for 15 minutes with 30 mg selenium powder at 600 mbar pressures. At lower temperature of 200 ºC, when annealing was carried out for 15 minutes with 30 mg selenium powder at 600 mbar pressure, the crystallite size was found to be 58 nm. This might be due to the absence of optimum temperature to cause inter-reaction amongst the elements and growth of the crystallites [36]. The precursor soft annealed at 225 ºC for 15 minutes at 600 mbar was found out to have least crystallite size of 42 nm. This was caused by selenium loss from precursor during annealing. The lattice parameters are calculated to be a=11.6684 Å, b=11.7509 Å, c=3.9503 Å in all the cases, indicating the presence of orthorhombic $Sb_2Se_3$[17].

### 4.2.2. Raman analysis

Raman spectra were recorded for $Sb_2Se_3$ thin films annealed at various temperatures and with different selenium content and is shown in figure 43. Laser of wavelength 532 nm is used to measure the Raman spectra.

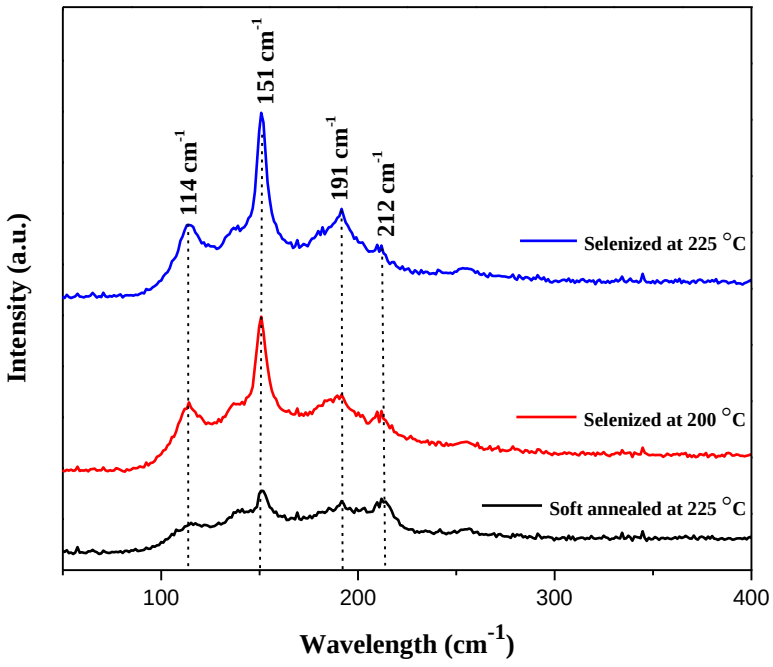


**Figure 43: Raman spectra of $Sb_2Se_3$ thin films annealed at various temperatures and with different selenium content**

The characteristics peaks were observed at 114 $cm^{-1}$, 151 $cm^{-1}$ and 191 $cm^{-1}$ for all of the annealed samples [29]. A weak intense peak was observed at 212 $cm^{-1}$ for all the samples. The highly intense peak at 151 $cm^{-1}$ is associated with Sb-Sb bond with $B_{2g}$ mode of vibration. The intense peak at 191 $cm^{-1}$ refers to heteropolar Sb-Se bond, corresponding to $A_g$ vibration mode. The peak at 212 $cm^{-1}$ corresponds to Se-Se bond of $A_g$ mode. The low intense peak at 114 $cm^{-1}$ refers to $B_{2g}$ mode of vibration [29]. The Raman peaks are highly intense for the sample annealed with 30 mg of selenium at 225 ºC for 15 minutes at 600 mbar pressure. While it is less for the sample annealed at 200 ºC with 30 mg of selenium for 15 minutes at 600 mbar pressure and it is least intense for the sample annealed in absence of selenium at 225 ºC for 15 minutes at 600 mbar pressure. The improvement in crystallinity is achieved at the optimum temperature and optimum time i.e. selenized at 225 ºC with 30 mg selenium for 15 minutes [29].

## 4.3. Morphological analysis

Figure 44 shows the surface morphology of $Sb_2Se_3$ thin film annealed with 30 mg of selenium at 200 ºC for 15 minutes at 600 mbar pressure. The reduction in temperature resulted in rod-shaped grain growth. The grain growth was found to be non-uniform and its size was calculated to be ~ 262 nm.

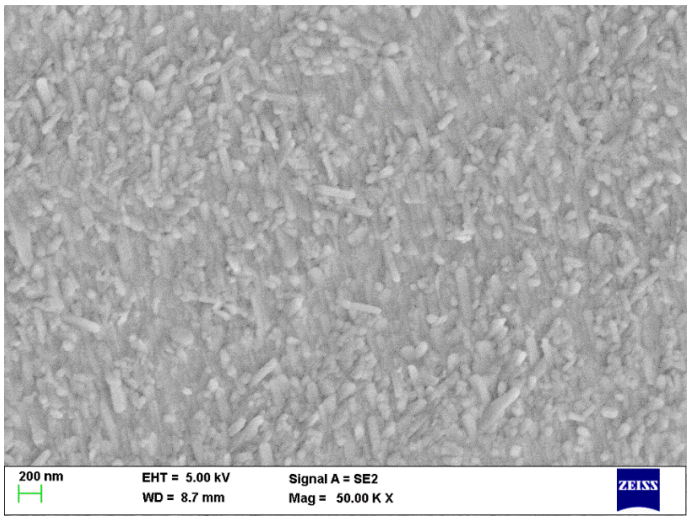


**Figure 44: SEM image of $Sb_2Se_3$ annealed at 200 ºC with 30 mg selenium for 15 minutes at 600 mbar pressure**

Figure 45 shows the surface morphology of $Sb_2Se_3$ thin film annealed with 30 mg of selenium at 225 ºC for 15 minutes at 600 mbar pressure. The surface morphology indicates uniform growth of the grains. The grains are sized of ~ 554 nm.

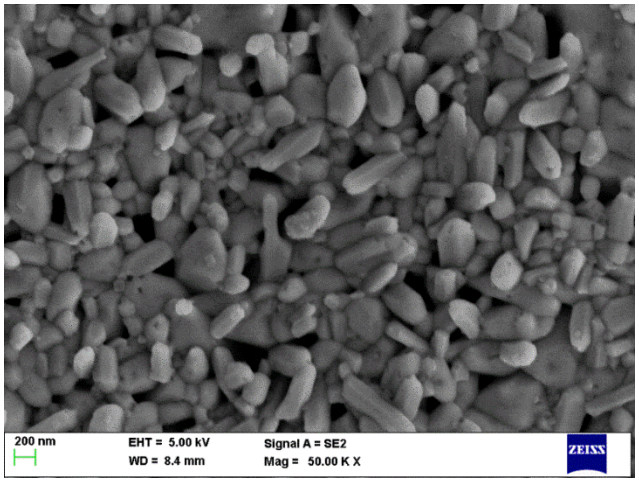


**Figure 45: SEM image of $Sb_2Se_3$ annealed at 225 ºC with 30 mg selenium for 15 minutes at 600 mbar pressure**

Figure 46 shows the surface morphology of $Sb_2Se_3$ thin film soft annealed at 225 ºC for 15 minutes at 600 mbar pressure. The grain growth became more non-uniform. The grain size was calculated to be ~ 203 nm. This might be due to the selenium loss during the annealing process, as clearly observed from compositional analysis.

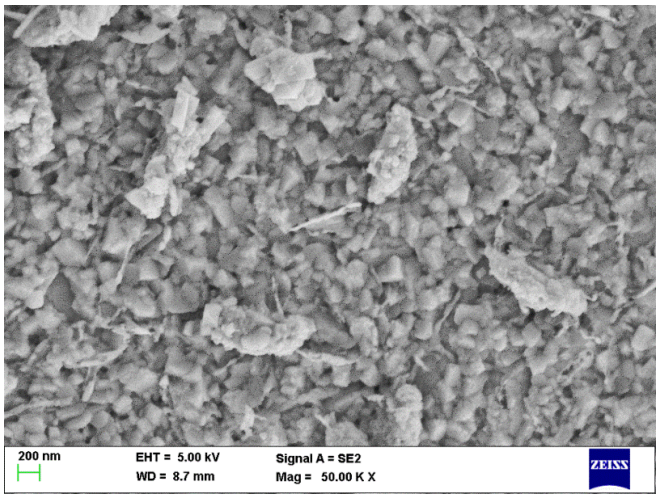


**Figure 46: SEM images of $Sb_2Se_3$ soft annealed at 225 ºC for 15 minutes at 600 mbar pressure**

The grain growth of the thin film selenized at 225 ºC with 30 mg selenium for 15 minutes at 600 mbar pressure was found to be uniform and dense than the thin films annealed at lower temperature and in absence of selenium.

## 4.4. Thickness measurement

The thickness of the $Sb_2Se_3$ thin films, selenized at different temperatures and with different selenium content was measured by using Taylor Hobson Stylus profiler of Talysurf CCI model. Table 8 shows the observed thicknesses of respective samples.

**Table 8: Thickness measurements of $Sb_2Se_3$ thin films annealed at different parameters**

| Annealing condition | Amount of selenium | Film thickness |
|---|---|---|
| 225 ºC-15 min-600 mbar | 30 mg | 480 nm |
| 200 ºC- 15 min-600 mbar | 30 mg | 444 nm |
| 225 ºC- 15min- 600 mbar | 0 mg | 330 nm |

The $Sb_2Se_3$ thin films annealed at 225 ºC in presence of 30 mg selenium for 15 minutes at 600 mbar pressure showed larger thickness in comparison to film annealed at other parameters. This might be due to the incorporation of selenium during the annealing process. The $Sb_2Se_3$ thin film selenized at 200 ºC in presence of 30 mg selenium for 15 minutes at 600 mbar pressure shows 444 nm followed by $Sb_2Se_3$ thin film soft annealed at 225 ºC for 15 minutes at 600 mbar pressure. The reason for less thickness might be the evaporation of selenium from the precursor and absence of extra selenium to compensate it. The thickness profile of the thin film selenized with 30 mg of selenium powder at 225 ºC for 15 minutes at 600 mbar pressure is shown in figure 47.

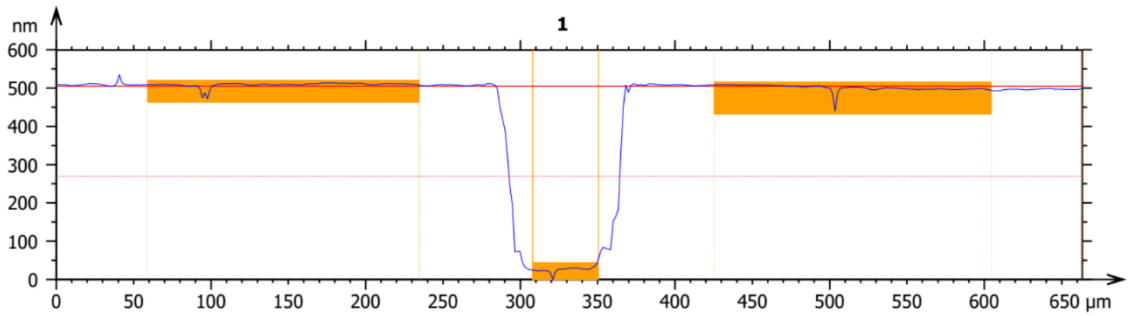


**Figure 47: Surface profile and thickness of $Sb_2Se_3$ thin film selenized with 30 mg of Se at 225 ºC for 15 minutes a d 600 mbar pressure by optical profilometer**

## 4.5. Optical Analysis

UV-Vis-NIR spectra is recorded using JACSO V770 in continuous scan mode with scan speed of 200 nm/min. Spectra data is recorded from wavelength of 2500 nm- 400 nm**.**

The reflectance data has been plotted using OriginPro 9.0 and the plot is shown in figure 48. The reflectance (R %) of sample soft annealed at 225 ºC for 15 min at 600 mbar pressure showed higher values in comparison to other samples. This can be attributed to the selenium loss from the precursor and inability to compensate the same from any other source. Hence, the sample is showing metallic property. The other samples had almost similar nature in their reflectance spectra.

**Energy band gap determination of annealed films using Tauc Plot:**

The optical band gap of the annealed thin films was determined by constructing a Tauc plot based on the Kubelka-Munk function as shown in figures 49-51. Table 9 shows the calculated energy bandgap of thin films grown at different parameters. The energy band gap values obtained in the range of 1.00 - 1.08 eV showing the presence of $Sb_2Se_3$ [17, 18]. The sample selenized in presence of 30 mg selenium at 200 ºC for 15 min at 600 mbar pressure shows bandgap of 1.00 eV. This might be due to presence of unreacted selenium at low temperature. The sample selenized in presence of 30 mg selenium at 225 ºC for 15 min at 600 mbar pressure shows bandgap of 1.07 eV. The energy band gap of the sample soft annealed at 225 ºC lies at 1.08 eV. The sample soft annealed at 225 ºC had higher band gap indicating the absence of selenium content, hence causing the sample to be more metallic. The metallic nature seemed to be reduced when the sample is selenized in presence of 30 mg selenium.

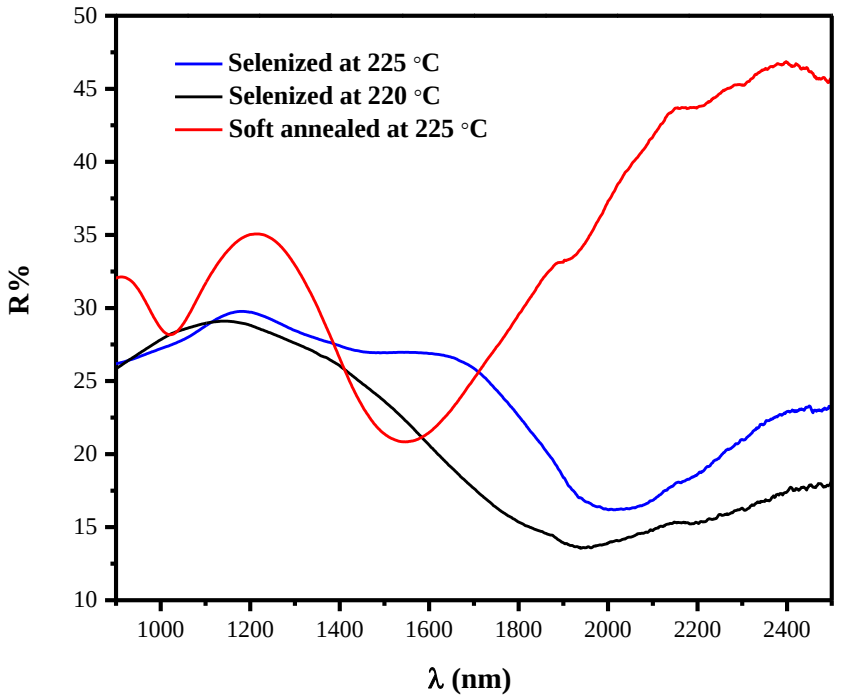


**Figure 48: Reflectance spectra of $Sb_2Se_3$ thin films annealed at different parameters**

**Table 9: Energy band gap of $Sb_2Se_3$ thin films annealed at different parameters**

| Annealing conditions | Amount of Selenium | Energy band gap of $Sb_2Se_3$ |
|---|---|---|
| 200 ºC-15 min-600 mbar | 30 mg | 1.00 eV |
| 225 ºC- 15 min-600 mbar | 30 mg | 1.07 eV |
| 225 ºC- 15min- 600 mbar | 0 mg | 1.08 eV |

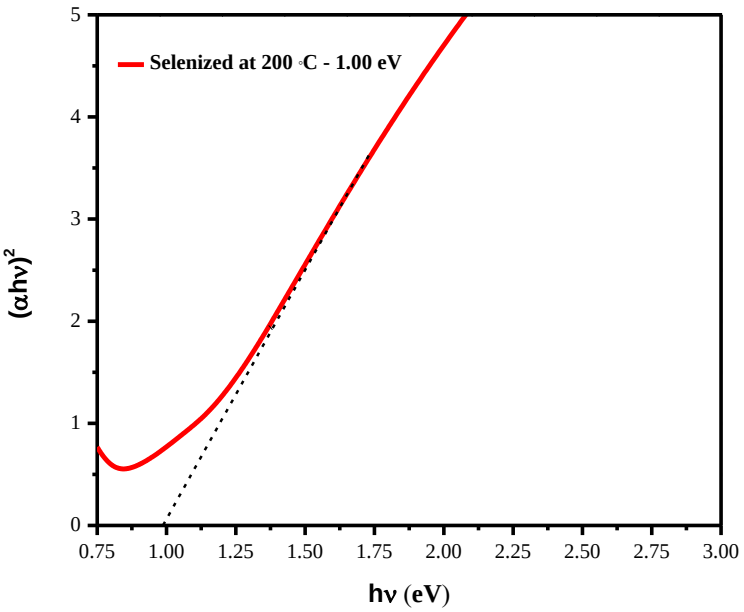


**Figure 49: Tauc plot of $Sb_2Se_3$ thin films annealed in presence of 30 mg selenium 200 ºC for 15 min at 600 mbar using Kubelka-Munk function**

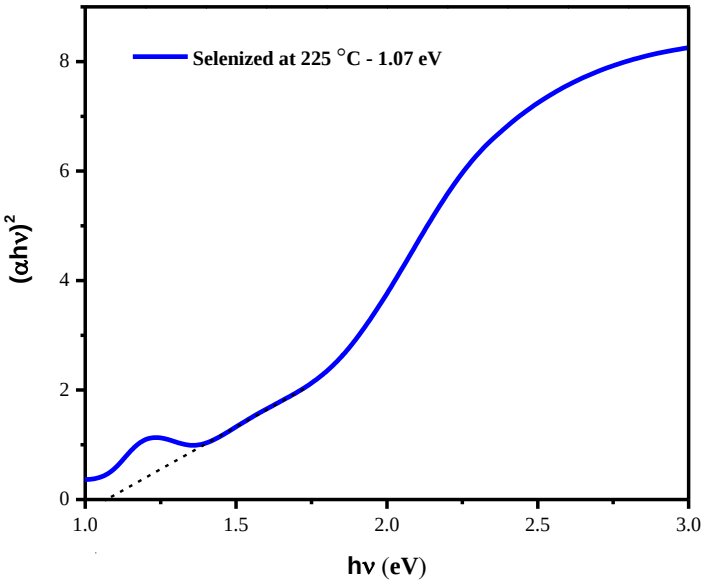


**Figure 50: Tauc plot of $Sb_2Se_3$ thin films annealed in presence of 30 mg selenium 225 ºC for 15 min at 600 mbar using Kubelka-Munk function**

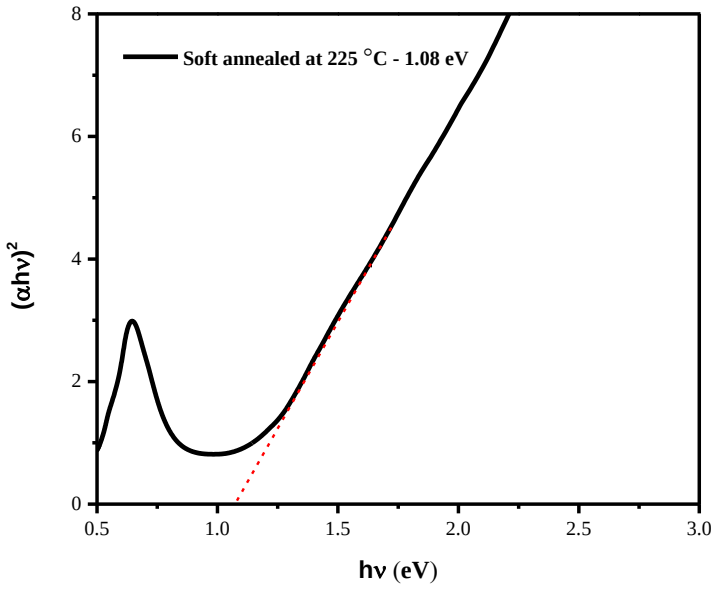


**Figure 51: Tauc plot of $Sb_2Se_3$ thin films soft annealed at 225 ºC for 15 min at 600 mbar using Kubelka-Munk function**

## 4.6. Electrical properties

Hall-effect measurement revealed the carrier concentration, carrier mobility, resistivity and the type of conductivity of the grown $Sb_2Se_3$ thin films. Table 10 shows the data extracted from the Hall-effect measurement for respective samples.

**Table 10: Electrical properties of $Sb_2Se_3$ thin films annealed at different parameters**

| Annealing conditions | Amount of Selenium | Carrier concentration ($cm^{-3}$) | Mobility ($cm^2/Vs$) | Resistivity (Ω cm) | Type |
|---|---|---|---|---|---|
| 225 ºC-15 min-600 mbar | 30 mg | $3.898\times10^{17}$ | $1.2\times10^{3}$ | $1.325\times10^{-2}$ | *p*-type |
| 200 ºC- 15 min-600 mbar | 30 mg | $6.568\times10^{19}$ | $1.1\times10^{2}$ | $8.643\times10^{-4}$ | *p*-type |
| 225 ºC- 15min-600 mbar | 0 mg | $1.445\times10^{20}$ | $2.0\times10^{1}$ | $3.894\times10^{-4}$ | *p*-type |

To measure electrical properties of annealed thin films Magnetic field of 1 Tesla and current of 100 μA is applied. Hall effect measurements revealed *p*-type conductivity in all $Sb_2Se_3$ thin films annealed under different conditions. The sample selenized in presence of 30 mg selenium at 225 ºC for 15 min at 600 mbar pressure exhibited carrier concentration of $3.898\times10^{17}$ $cm^{-3}$, mobility of $1.2\times10^{3}$ $cm^2/Vs$ and resistivity of $1.325\times10^{-2}$ Ω cm. This sample was found out to have the highest mobility amongst all the samples. The resistivity value indicated its semiconducting nature. The sample selenized in presence of 30 mg selenium at 200 ºC for 15 min at 600 mbar pressure showed carrier concentration of $6.568\times10^{19}$ $cm^{-3}$, mobility of $1.1\times10^{2}$ $cm^2/Vs$ and resistivity of $8.643\times10^{-4}$ Ω cm. The sample soft annealed at 225 ºC for 15 min at 600 mbar pressure exhibited carrier concentration of $1.445\times10^{20}$ $cm^{-3}$, mobility of $2.010\times10^{2}$ $cm^2/Vs$ and resistivity of $3.894\times10^{-4}$ Ω cm. It has been observed that increase in temperature led to decrease in carrier concentration, increase in mobility and increased the resistivity of the sample. Better incorporation of selenium took place on increasing the annealing temperature, causing the compound to become more semiconducting in nature. Soft annealing led to loss of selenium, that attributed to its metallic nature as well as poor semiconducting properties in comparison to the sample selenized at same temperature. Hence sample selenized at 225 ºC for 15 minutes with 30 mg selenium for 600 mbar pressure was found to have the best electrical properties amongst the annealed samples.

# CHAPTER 5: CONCLUSION

## 5.1. Summary and conclusion

The purpose of the project was to grow $Sb_2Se_3$ thin films using stacked elemental layers via electron beam deposition method. The prepared thin films were annealed at various conditions to make it convenient for application as an absorber layer in solar cells. Firstly, the precursors were selenized using 30 mg of selenium at 200 ºC for 15 minutes at 600 mbar pressure. Then the precursors were selenized in presence of 30 mg selenium at 225 ºC for 15 minutes at 600 mbar pressure. Above this temperature, the precursors were unstable. Hence, soft annealing of precursors was done at 225 ºC for 15 minutes at 600 mbar pressure. Out of all the annealed thin films, the thin film selenized at 225 ºC for 15 minutes at 600 mbar pressure with 30 mg selenium powder was found to have better morphological and compositional results with near stoichiometric composition. The XRD results of the sample revealed singular phases of $Sb_2Se_3$ at 28.26º, 31.24º and 38.88º corresponding to the planes (2 1 1), (2 2 1), (1 4 1) respectively. The films were found to have orthorhombic structure, with lattice parameters a = 11.6684 Å, b = 11.7509 Å, c = 3.9503 Å. Raman spectra also confirmed the peaks of $Sb_2Se_3$ compound. The SEM analysis revealed the grain size to be ~ 554 nm. The thickness of the thin film, selenized in presence of 30 mg selenium at 225 ºC for 15 minutes at 600 mbar was found to be 480 nm. The optical band gaps of the samples were found out to be in the range of 1.00- 1.08 eV. The metallic nature of the sample decrease as we incorporate selenium additionally through selenization. The electrical property is found to be better for the sample selenized in presence of 30 mg selenium at 225 ºC for 15 minutes at 600 mbar. The sample exhibited carrier concentration of $3.898\times10^{17}$ $cm^{-3}$, mobility of $1.2\times10^{3}$ $cm^2/Vs$ and resistivity of $1.325\times10^{-2}$ Ω cm.

## 5.2. Future Scope

In this present work, $Sb_2Se_3$ thin film is characterized as a *p*-type material, which makes it a good absorber layer. By using *n*-type material (example- CdS, ZnS, ZnO) as a window layer along with the synthesized *p*-type $Sb_2Se_3$ thin film, a solar cell might be prepared with desirable power conversion efficiency.

# REFERENCES

[1] R. Foster, M. Ghassemi, and A. Cota, “Solar Energy,” Aug. 2009, doi: https://doi.org/10.1201/9781420075670.

[2] Smets, A., Jäger, K., Isabella, O., Van Swaaij, R., & Zeman, M. (2016). Solar Energy: “The physics and engineering of photovoltaic conversion, technologies and systems”. Bloomsbury Publishing.

[3] I. B. Fridleifsson, “Geothermal energy for the benefit of the people,” Renewable and Sustainable Energy Reviews, vol. 5, no. 3, pp. 299–312, Sep. 2001, doi: https://doi.org/10.1016/s1364-0321(01)00002-8.

[4] J. Cheng, “Biomass to Renewable Energy Processes”, Second Edition. CRC Press, 2017. doi: https://doi.org/10.1201/9781315152868.

[5] G. M. Joselin Herbert, S. Iniyan, E. Sreevalsan, and S. Rajapandian, “A review of wind energy technologies,” Renewable and Sustainable Energy Reviews, vol. 11, no. 6, pp. 1117–1145, Aug. 2007, doi: https://doi.org/10.1016/j.rser.2005.08.004.

[6] A. Smets, Klaus Jäger, O. Isabella, René van Swaaij, and M. Zeman, “Solar Energy”. Bloomsbury Publishing, 2016.

[7] Fahrenbruch, Alan, and Richard Bube. “Fundamentals of solar cells: photovoltaic solar energy conversion”. Elsevier, 2012.

[8] K. Raut, H. Chopde, and D. Deshmukh, “A Review on Comparative Studies of Diverse Generation in Solar Cell,” International Journal of Electrical Engineering and Ethics, vol. 1, 2018, Available: http://www.ijeeejournal.org/Volume1/Issue3/IJEEE-V1I3P1.pdf

[9] M. Schmid, “Revisiting the Definition of Solar Cell Generations,” Advanced Optical Materials, Aug. 2023, doi: https://doi.org/10.1002/adom.202300697

[10] T. D. Lee and A. U. Ebong, “A review of thin film solar cell technologies and challenges,” Renewable and Sustainable Energy Reviews, vol. 70, pp. 1286–1297, Apr. 2017, doi: https://doi.org/10.1016/j.rser.2016.12.028.

[11] Md. K. S. Bin Rafiq et al., "WS2: A New Window Layer Material for Solar Cell Application," Scientific Reports, vol. 10, no. 1, Jan. 2020, doi: https://doi.org/10.1038/s41598-020-57596-5

[12] "Optical Absorption-Solar Cell and Photodetectors – Semiconductor material and devices," Inflibnet.ac.in, 2025. https://ebooks.inflibnet.ac.in/msp10/chapter/optical-absorption-solar-cell-and-photodetectors/ (accessed Mar. 19, 2025).

[13] S. M. Sze, "Semiconductor devices physics and technology", pp. 124-126, 2nd edition, Wiley-India edition, 2008.

[14] A. Khamis, N. I. M. Rodzi, and N. Z. A. Naharuddin, "Absorber layer improvement and performance analysis of CIGS thin-film solar cell," Journal of Ovonic Research, vol. 20, no. 3, pp. 309–323, May 2024, doi: https://doi.org/10.15251/jor.2024.203.309

[15]. P. Reinhard et al., "Review of progress toward 20% efficiency flexible CIGS solar cells and manufacturing issues of solar modules," IEEE Xplore, Jun. 01, 2012. https://ieeexplore.ieee.org/abstract/document/6656789

[16] Manaf Zghaibeh et al., "CdTe solar cells fabrication and examination techniques: a focused review," International Journal of Green Energy, vol. 20, no. 5, pp. 555–570, Sep. 2022, doi: https://doi.org/10.1080/15435075.2022.2126943.

[17] A. Mavlonov *et al.*, "A review of $Sb_2Se_3$ photovoltaic absorber materials and thin-film solar cells," *Solar Energy*, vol. 201, pp. 227–246, May 2020, doi: https://doi.org/10.1016/j.solener.2020.03.009.

[18] T. M. Razykov, A. X. Shukurov, O. K. Atabayev, K. M. Kuchkarov, B. Ergashev, and A. A. Mavlonov, "Growth and characterization of $Sb_2Se_3$ thin films for solar cells," *Solar Energy*, vol. 173, pp. 225–228, Oct. 2018, doi: https://doi.org/10.1016/j.solener.2018.07.082.

[19] Rokas Kondrotas, J. Zhang, C. Wang, and J. Tang, "Growth mechanism of $Sb_2Se_3$ thin films for photovoltaic application by vapor transport deposition," vol. 199, pp. 16–23.

[20] K. J. Tiwari, Min Qin Ren, Saumitra Kamalakar Vajandar, T. Osipowicz, A. Subrahmanyam, and P. Malar, "Mechanochemical bulk synthesis and e-beam growth of

thin films of Sb2Se3 photovoltaic absorber," Solar Energy, vol. 160, pp. 56–63, Jan. 2018, doi: https://doi.org/10.1016/j.solener.2017.11.074.

[21] V. Kumar, E. Artegiani, A. Kumar, G. Mariotto, F. Piccinelli, and A. Romeo, "Effects of post-deposition annealing and copper inclusion in superstrate $Sb_2Se_3$ based solar cells by thermal evaporation," Solar Energy, vol. 193, pp. 452–457, Nov. 2019, doi: https://doi.org/10.1016/j.solener.2019.09.069.

[22] S. Ghosh, M. V. B. Moreira, C. Fantini, and J. C. González, "Growth and optical properties of nanocrystalline $Sb_2Se_3$ thin-films for the application in solar-cells," Solar Energy, vol. 211, pp. 613–621, Nov. 2020, doi: https://doi.org/10.1016/j.solener.2020.10.001.

[23] None Mamta, K.K. Maurya, and V. N. Singh, "$Sb_2Se_3$ versus Sb2S3 solar cell: A numerical simulation," Solar Energy, vol. 228, pp. 540–549, Oct. 2021, doi: https://doi.org/10.1016/j.solener.2021.09.080.

[24] L. Lin, Y. Qiu, and B. Fan, "Analysis of $Sb_2Se_3$/CdS based photovoltaic cell: A numerical simulation approach," vol. 122, pp. 19–24, Nov. 2018, doi: https://doi.org/10.1016/j.jpcs.2018.05.045.

[25] Z. Wang and Z. Zhang, "Electron Beam Evaporation Deposition," pp. 33–58, Sep. 2016, doi: https://doi.org/10.1002/9783527696406.ch2.

[26] Hata, David M., Elena V. Brewer, and Nancy J. Louwagie. Introduction to Vacuum technology. Milne Open Textbooks, 2023.

[27] L. Ward, "Introduction to high vacuum technology", pp-40-95, Wiley-Indian edition,1998

[28] Marx KA." Quartz crystal microbalance: a useful tool for studying thin polymer films and complex biomolecular systems at the solution− surface interface". Biomacromolecules. 2003 Sep 8;4(5):1099-120.

[29] B. Srinivas, S. Babujani, G. H. Chandra, Y. P. V. Subbaiah, and M. Gupta, "Synthesis and characterization of Cu-sandwiched $Sb_2Se_3$ thin films and numerical simulation of p-$Sb_2Se_3$/n-ZnSe heterojunction solar cell," Optical Materials, vol. 135, p. 113289, Jan. 2023, doi: https://doi.org/10.1016/j.optmat.2022.113289.

[30] Daniel. Abou-Ras, Thomas. Kirchartz, and Uwe. Rau, Advanced Characterization Techniques for Thin Film Solar Cells. Wiley-VCH, 2011.

[31] Fatimah, Siti, et al. "How to calculate crystallite size from x-ray diffraction (XRD) using Scherrer method." ASEAN Journal of Science and Engineering 2.1 (2022): 65-76.

[32] Ai, Ask. "UV-Vis Spectroscopy–Principle, Instrumentation, Applications, Advantages, and Limitation."

[33] Deen, M. Jamal, and Fabien Pascal. "Electrical characterization of semiconductor materials and devices." Journal of Materials Science: Materials in Electronics 17 (2006): 549-575.

[34] Leng, Yang. “Materials characterization: introduction to microscopic and spectroscopic methods”. pp-55-60, John Wiley & Sons, 2013.

[35] Siderov, V. & Mladenova, D. & Yordanov, Rumen & Milenkov, V. & Ohlídal, Miloslav & Salyk, Ota & Zhivkov, I. & Weiter, Martin. (2013). Film thickness measurement by optical profilometer MicroProf® FRT. Bulgarian Chemical Communications. 45. 194-197.

[36] Saritha, K., G. Phaneendra Reddy, and KT Ramakrishna Reddy. "The Effect of Selenization Temperature on Morphological and Structural Properties of Tin Diselenide Thin Films Grown by a Two-Stage Process." transition 4 (2015): 9.